## COMPUTATIONAL SHOCK FORMATION FOR THE MULTI-DIMENSIONAL EULER EQUATIONS

#### GAVIN PANDYA, STEVE SHKOLLER, AND VLAD VICOL

ABSTRACT. Based on Arbitrary Lagrangian Eulerian (ALE) coordinates, adapted to the fast acoustic characteristic surfaces, and a new class of Differentiated Riemann Variables (DRV) that were devised in [8], we introduce a 4th-order accurate *Computational Shock Formation* (CSF) algorithm. Smooth, locally compressive, and generic initial conditions form discontinuous shockwaves, but prior to the development of such a surface of discontinuity, a spacetime codimension-2 manifold is formed. This manifold, called a *pre-shock* set consists of all spacetime points at which the gradient of the Euler solution has first become infinite. Specifically, from smooth and compressive data, the Euler solution first forms a  $C^{1/3}$  solution, with the cusp forming along this pre-shock manifold of gradient catastrophes. It is directly from the *pre-shock* set, that the discontinuous shock surface develops. By a transformation of spacetime which flattens the pre-shock manifold onto a horizontal time-slice, our CSF algorithm uses DRV in ALE coordinates to accurately compute the pre-shock manifold, and as well as the  $C^{1/3}$  Euler solution about this pre-shock set. This is essential for the problem of *Computational Shock Development*.

#### **CONTENTS**

1. Introduction	1
2. Differentiated Riemann variables in two space dimensions	5
3. Euler in ALE coordinates adapted to fast acoustic characteristic surfaces	10
4. A precursor to the Computational Shock Formation Algorithm	17
5. The Computational Shock Formation Algorithm	25
Appendix A. Numerical computation of the coefficients of the Puiseux expansions	30
Acknowledgements	31
References	31

#### 1. Introduction

Solutions to the Euler equations of gas dynamics exhibit extraordinarily varied qualitative features that depend on the initial conditions being either smooth or discontinuous. Most modern numerical schemes for Euler have been designed to accurately simulate the propagation of shock waves, contact discontinuities, and rarefaction fans that arise from discontinuous data. On the other hand, for smooth and compressive initial data, solutions to the Euler equations evolve towards shockwaves and "weak characteristic discontinuities" and produce fine-scale cusp structures which most computational algorithms are not equipped to simulate.

As has been proven in [8], generically, starting from smooth and locally compressive initial conditions, sound waves propagate, forming sharper and sharper fronts, until a succession of (Eulerian) gradient catastrophes occur, from which the discontinuous shockwaves emerge. Specifically, smooth and steepening sound waves first form a  $C^{\frac{1}{3}}$  cusp-type solution along a spacetime manifold called the *pre-shock* set, a collection of points in spacetime where the gradient of the Euler solution has become infinite, but the solution itself remains continuous. From this pre-shock manifold, the discontinuous shock surface develops instantaneously. Landau & Lifschitz [5, Chapter IX, §96] conjectured that together with the emergence of the discontinuous shock wave, two other "weak characteristic discontinuities" simultaneously emerge from this pre-shock manifold. This was proven to be true in [1]; in addition to the shock wave, there exists a slow acoustic characteristic surface and a vorticity-carrying (and entropy-carrying) characteristic surface that both emanate from this pre-shock set. The former is called the weak rarefaction wave and the latter is referred to as the weak contact discontinuity. Together, these three surfaces that emanate from the pre-shock set split the spacetime into four regions, each with its own solution structure. While it is well-known that Euler solutions experience entropy-producing jump discontinuities across the shock front, it has only recently been established in [1] that gradients of the Euler solution produce  $C^{\frac{1}{2}}$  cusp singularities along the weak contact and rarefaction surfaces, which explains the "weak characteristic discontinuities" terminology of Landau & Lifschitz. High-order numerical methods

1

for gas dynamics have not been optimized to accurately reproduce the locations of such characteristic surfaces nor to capture the associated fine-scale cusp structures, which do not exist in Riemann problems or in solutions that evolve discontinuous data. To be precise, in order to accurately approximate the emergent derivative-cusp structure and the weak characteristic discontinuities that emerge from smooth data, it is first essential to accurately compute the precise location and structure of the pre-shock manifold of first gradient catastrophes, and to accurately compute the  $C^{\frac{1}{3}}$  Euler solution about this pre-shock set. We shall refer to the numerical propagation of smooth, generic, and compressive initial conditions up to the pre-shock manifold as  $Computational\ Shock\ Formation\ (CSF)$ . The numerical solution of the Euler equations that uses the pre-shock manifold as the initial Cauchy surface and evolves the discontinuous shock wave solution that emanates from this pre-shock set is termed  $Computational\ Shock\ Development\ (CSD)$ .

Our focus in this work is the development of a 4th-order accurate numerical algorithm for *Computational Shock Formation* for solutions of the Euler equations in two space dimensions:<sup>1</sup>

$$\partial_t(\rho \mathbf{u}) + \operatorname{div}(\rho \mathbf{u} \otimes \mathbf{u} + p\mathbf{I}) = 0,$$
 (1.1a)

$$\partial_t \rho + \operatorname{div}(\rho \mathbf{u}) = 0, \tag{1.1b}$$

$$\partial_t E + \operatorname{div}(\boldsymbol{u}(E+p)) = 0,$$
 (1.1c)

where the pressure  $p=(\gamma-1)\left(E-\frac{1}{2}\rho|\boldsymbol{u}|^2\right)$  is related to energy, density, and velocity of the ideal gas law and  $\gamma>1$  is the adiabatic exponent. Here,  $\boldsymbol{u}=(u^1,u^2)$  denotes the fluid velocity vector field,  $\rho$  is the strictly positive density function, and E is the total energy. Prior to the formation of discontinuous shocks, conservation of energy (1.1c) can be replaced with the transport of specific entropy s,

$$\partial_t s + \boldsymbol{u} \cdot \nabla s = 0, \tag{1.1c'}$$

in which case the pressure can be expressed as a function of entropy and density by

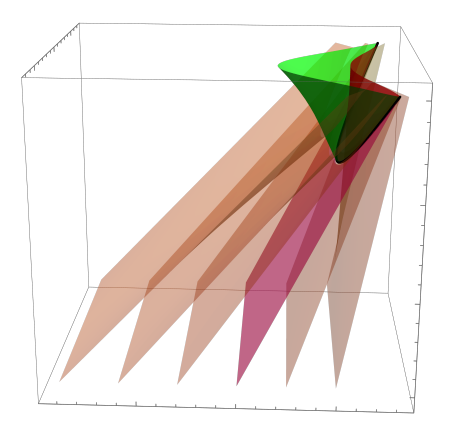
$$p(s,\rho) = \frac{1}{\gamma} \rho^{\gamma} e^{s}$$
.

1.1. Shock formation in compressible Euler. The mechanism of shock formation by the steepening of sound waves can be viewed geometrically as the narrowing distance between nearby fast acoustic characteristic surfaces. Compression in the initial conditions is determined by large negative slopes present in at least one of the state variables. Initial conditions are termed generic if a large negative slope has a non-degenerate local minimum. In a neighborhood of such a local minimum, in which the slope is negative, the fast acoustic characteristics emanating from such a neighborhood evolve towards one another and impinge in finite time. The nature of the local minimum of the negative slope in the initial data produces a unique time and spatial location for the first such impingement of nearby characteristic surfaces. This time coincides with  $t = T^*$ , the time of the first gradient blowup of the Eulerian state variables, and the spatial coordinate  $y^* = (y_1^*, y_2^*)$  (of this first characteristic impingement) corresponds to the location of the first gradient blowup. Geometrically, the spacetime point  $(y^*, T^*)$  is the minimum of the spacetime pre-shock curve that was described above. We refer the reader to [2–4] for a detailed analysis of shock formation for the multi-dimensional Euler equations up to the spacetime location  $(y^*, T^*)$  and to [8] for a the analysis of the Euler shock formation process (well past the time  $t = T^*$  of first gradient singularity) up to the boundary of the Maximal Globally Hyperbolic Development (MGHD), the largest possible spacetime set on which the Euler solution remains smooths, and in which characteristic flows are invertible.

In order to explain our geometric framework for shock formation, it is convenient to choose initial conditions and coordinates  $(x_1,x_2)$  in such a way that the largest negative slope of our state variables occurs along the  $x_1$ -axis, resulting in sound waves initiating their steepening process as they propagate in this direction. As time evolves, the distance between fast acoustic characteristic surfaces, that at initial time  $t=t_{\rm in}$  are parallel to the transverse  $x_2$ -direction, begins to narrow and eventually converges to zero. This is displayed in Figure 1, where in the left panel, we show the spacetime set in Eulerian coordinates. The horizontal plane bounding the spacetime box from below denotes the initial time-slice  $\{t=t_{\rm in}\}$  with coordinates  $(x_1,x_2)$  (for the two-dimensional periodic spatial domain), while the vertical axis has time t as the coordinate. Six characteristic surfaces are shown to impinge as they evolve (upwards) in time onto the surface of first singularities. This surface consists of the pre-shock curve (shown in black) together with the singular surface (shown in red) which emanates from the pre-shock in the downstream direction and consists of a continuum of gradient catastrophes. The slow acoustic characteristic surface (shown in green), which also emanates from the pre-shock in the upstream direction, is a Cauchy horizon which the Euler solution can never reach.

<sup>&</sup>lt;sup>1</sup>In almost the identical manner, our computational shock formation algorithm can be implemented for the Euler equations in three space dimensions.

<sup>&</sup>lt;sup>2</sup>A local minimum is non-degenerate if the second-derivative test from calculus can be applied.



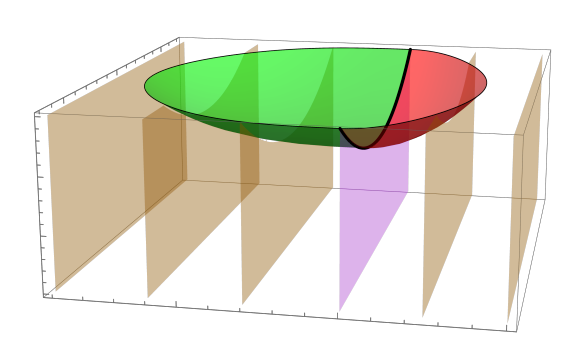


FIGURE 1. (Left). Spacetime in Eulerian coordinates. The characteristic surfaces are shown to impinge on the surface of first singularities, which consists of the pre-shock curve (black) together with the singular surface (red) which emanates from the pre-shock in the downstream direction and consists of a continuum of gradient catastrophes. The slow acoustic characteristic surface (green) which emanates from the pre-shock in the upstream direction is a Cauchy horizon which the Euler solution can never reach. (Right). The spacetime in Arbitrary Lagrangian Eulerian (ALE) coordinates denotes the region below the union of the ALE pre-shock curve (black), the ALE singular set (red), and the ALE slow characteristic surface (green). In ALE coordinates, each fast acoustic characteristic surface has been flattened. The surface shown in magenta denotes the fast acoustic characteristic surface that passes through the pre-shock curve.

In the right panel of Figure 1, we display the evolution of the same six characteristic surfaces, but in Arbitrary Lagrangian Eulerian (ALE) coordinates which have been adapted to the fast wave speed. Specifically, the ALE coordinates (which we will discuss below) are chosen to "freeze" the fast characteristics and (vertically) flatten those surfaces. We display the ALE pre-shock curve (black), the ALE singular set surface (red), and the ALE slow characteristic surface (green). In both the left and the right panels, the surface shown in magenta denotes the unique fast acoustic characteristic surface that passes through the pre-shock curve.

The horizontal plane bounding the spacetime box from above is the final time-slice of the dynamics  $\{t=t_{\rm fin}\}$ . The spacetime lying underneath the surface consisting of the union of the green Cauchy horizon, the black pre-shock curve, the red singular set surface, and the final time-slice, is the largest spacetime, contained in the box  $\mathbb{T}^2 \times [t_{\rm in}, t_{\rm fin}]$ , on which the Euler solution remains smooth, and all characteristic families remain invertible. We call this spacetime the *Maximal Globally Hyperbolic Development in a Box* (MGHD) of the smooth, locally compressive, and generic initial data that is prescribed on the initial time-slice  $\{t=t_{\rm in}\}$ .

The spacetime of the  $\overline{\text{MGHD}}$  is larger than the spacetime associated to the physical shockwave solution. The shock surface, which also emanates from the pre-shock curve, is tangential (along the pre-shock curve) to the singular set surface, but lies strictly underneath this singular set. Computationally, it is essential to evolve the Euler solution only up to the pre-shock curve (black curve in Figure 1), and to classify the Euler solution in an open neighborhood of this curve. We parameterize the pre-shock curve with time as a function of the transverse  $x_2$ -coordinate,  $t = t^*(x_2)$ , and the  $x_1$ -coordinate,  $x_1 = X_1^*(x_2)$ . By extending this parameterization as a constant in the  $x_1$ -direction, we define the cylindrical surface shown in orange in Figure 2, as the upper bound for largest spacetime set containing the physically-relevant smooth solution.

We design the *Computational Shock Formation* algorithm for the purpose of numerically evolving smooth, compressive, and generic initial data up to the cylindrical surface  $t = t^*(x_2)$  with 4th-order accuracy, and then computing a fractional-order Puiseux expansion for the Euler solution at each time  $t^*(x_2)$ .

1.2. The spacetime domain. A key challenge of computational shock formation in multiple space dimensions comes from the nontrivial time-dependence of the curve of pre-shocks, parameterized<sup>3</sup> by  $x_1 = X_1^*(x_2)$  and  $t = t^*(x_2)$  where the a priori unknown function  $t^*$  must be determined as part of the solution and depends upon the initial data. Standard differencing stencils provide can provide accurate approximations to the Euler solution only up to the time for the first gradient singularity, which is the minimum temporal value  $t = T^*$  on the curve of pre-shocks. As the

<sup>&</sup>lt;sup>3</sup>We shall provide a precise definition for the curve of pre-shocks and the parameterization  $x_1 = X_1^*(x_2)$  and  $t = t^*(x_2)$  in Section 3.5.1 below.

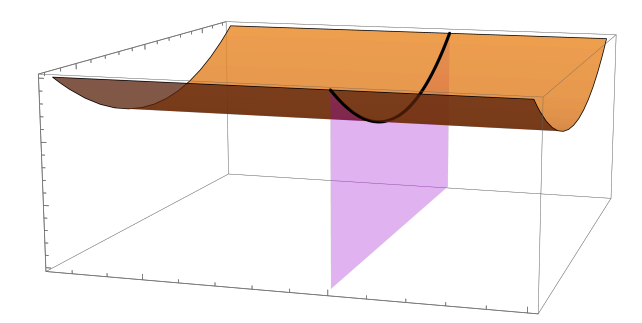


FIGURE 2. The ALE spacetime  $\Omega^* := \{x = (x_1, x_2, t) \colon x \in \mathbb{T}^2, \mathsf{t}_{\mathsf{in}} \leq t < t^*(x_2) \leq \mathsf{t}_{\mathsf{fin}} \}$  is displayed. The pre-shock curve  $(X_1^*(x_2), t^*(x_2))$  shown in black is extended as a constant-in- $x_1$  cylindrical surface shown in orange. Computational shock formation requires the evolution of the Euler solution up this cylindrical surface. The nearly vertical magenta surface intersects the curve of pre-shocks and separates spacetime into the upstream region (to the left) and the upstream region (to the right).

shock surface-of-discontinuity begins to emanate from this pre-shock curve for times  $t>T^*$ , traditional numerical algorithms are forced to employ shock-capturing methods which necessarily have only 1st-order accuracy at the shock. We shall take a different approach to the computation of the Euler solution in the ALE spacetime set

$$\Omega^* := \{ (\boldsymbol{x}, t) = (x_1, x_2, t) \colon \boldsymbol{x} \in \mathbb{T}^2, \mathsf{t}_{\mathsf{in}} \le t < t^*(x_2) \le \mathsf{t}_{\mathsf{fin}} \}, \tag{1.2}$$

shown in Figure 2 as the spacetime inside the box  $\mathbb{T}^2 \times [\mathsf{t}_{\mathsf{in}}, \mathsf{t}_{\mathsf{fin}}]$  and bounded above by the orange cylindrical surface  $t < t^*(x_2)$ . For smooth, locally compressive, and generic initial data, the Euler solution remains smooth in  $\Omega^*$ , and while the Eulerian gradient of the solution experiences a continuum of "first" blowup at  $t = t^*(x_2)$ , in the ALE coordinates that we shall define below, our CSF-computed solution remains smooth, even up to the boundary of this spacetime set. In order to numerically solve the Euler equations up to the cylindrical surface  $t = t^*(x_2)$ , we follow the spacetime remapping strategy introduced in [8] and define a temporal change-of-variables  $s = q(x_2, t)$  which flattens the cylindrical surface  $t = t^*(x_2)$  to the flat plane  $\{s = 1\}$  in (x, s) coordinates. The combination of this temporal remapping and a new ALE coordinate system allow us to compute the location of the pre-shock curve and the state variables about the pre-shock set with high-order accuracy.

1.3. **Notation.** ALE dependent variables are functions of the independent variables  $\boldsymbol{x}=(x_1,x_2)$  and t, and Eulerian dependent variables are functions of the independent variables  $\boldsymbol{y}=(y_1,y_2)$  and t. For both sets of dependent variables, the time coordinate may be replaced with remapped temporal coordinate s.

We shall write Eulerian functions with lowercase letters such w, z, or  $\sigma$ , and their ALE counterparts will be denoted by uppercase letters such as W, Z, or  $\Sigma$ . Hence, functional dependence for Eulerian functions will appear as w(y,t) and for ALE functions as W(x,t).

We shall use the following derivative notation: for a differentiable Eulerian function f(y,t), we write

$$f_{,k}(\boldsymbol{y},t) := \frac{\partial f}{\partial y^k}(\boldsymbol{y},t) \text{ for } k \in \{1,2\},$$

and similarly for a differentiable ALE function,

$$F_{,k}\left( oldsymbol{x},t
ight) :=rac{\partial F}{\partial x^{k}}(oldsymbol{x},t) \ \ ext{for} \ \ k\in\left\{ 1,2\right\} .$$

The notation  $\partial_k f(\boldsymbol{y},t)$  will also be used to mean  $f_{,k}(\boldsymbol{y},t)$  and  $\partial_k F(\boldsymbol{x},t)$  denotes  $F_{,k}(\boldsymbol{x},t)$ .

We use the Einstein summation convention in which repeated indices are summed from 1 to 2. For example,

$$u^{j},_{k} u^{i},_{j} := \sum_{j=1}^{2} \partial_{k} u^{j} \partial_{j} u^{i}$$
.

We will denote most vectors and matrices with bold font.

1.4. **Outline of the paper.** In Section 2, we derive the Differentiated Riemann Variables (DRV) that we shall use for CSF algorithm. These DRV provide a slight generalization of the variables introduced in [8]. As can be seen from the identity (2.16) below, these DRV are specific linear combinations of normal and tangential derivatives of classical Riemann variables and geometric curvature functions, a combination which is important to our algorithm. In Section 3 we present the Arbitrary Eulerian Lagrangian (ALE) coordinate system that is adapted to the fast acoustic

characteristic surfaces. Our algorithm uses our DRV functions in this ALE framework. Section 4 presents a 4th-order accurate numerical scheme design to accurately capture the spacetime location  $(y^*, T^*)$  of the first (Eulerian) gradient catastrophe and to accurately simulate the  $C^{\frac{1}{3}}$  Euler solution about this point. This algorithm is a precursor to our main result. In particular, in Section 5, we provide a detailed description of our *Computational Shock Formation* (CSF) algorithm, which allows us to evolve the Euler solution up to, and including the entire manifold of pre-shocks with 4th-order accuracy.

## 2. DIFFERENTIATED RIEMANN VARIABLES IN TWO SPACE DIMENSIONS

2.1. A symmetric form of the Euler equations. Our computational shock formation algorithm will make use of a generalization of the *differentiated Riemann variables* that were used in [8] for the problem of determining the  $\overline{\text{MGHD}}$ . To determine the precise structure of these variables, we shall first rewrite the Euler equations in a more symmetric form. With the sound speed c defined as

$$c^2 = \partial p / \partial \rho = \rho^{2\alpha} e^s \,,$$

we introduce the rescaled sound speed

$$\sigma = \frac{c}{\alpha}$$

where  $\alpha$  is the rescaled adiabatic exponent given by

$$\alpha = \frac{\gamma - 1}{2} \,. \tag{2.1}$$

Prior to the formation of discontinuous shockwaves, the Euler equations (1.1) can be the equivalently written in terms of the  $(u, \sigma, s)$  as the following system:

$$\partial_t \mathbf{u} + \mathbf{u} \cdot \nabla \mathbf{u} + \alpha \sigma \nabla \sigma = \frac{\alpha \sigma^2}{4\alpha + 2} \nabla s,$$
 (2.2a)

$$\partial_t \sigma + \boldsymbol{u} \cdot \nabla \sigma + \alpha \sigma \operatorname{div} \boldsymbol{u} = 0, \qquad (2.2b)$$

$$\partial_t s + \boldsymbol{u} \cdot \nabla s = 0. \tag{2.2c}$$

We shall avoid vacuum states and consider  $\sigma > 0$ .

2.2. Eigenspace of Euler. The system (2.2) can be written in the vector form

$$\partial_t \mathbf{q} + \mathbf{F}^i(\mathbf{q})\partial_i \mathbf{q} = 0, \tag{2.3}$$

where q = q(y, t) is the vector of state variables, and  $\mathbf{F}^{i}(q)$ , i = 1, 2, are the transport matrices given by

$$\mathbf{q} = \begin{pmatrix} u^{1} \\ u^{2} \\ \sigma \\ s \end{pmatrix}, \qquad \mathbf{F}^{1}(\mathbf{q}) = \begin{pmatrix} u^{1} & 0 & \alpha\sigma & \frac{-\alpha\sigma^{2}}{4\alpha+2} \\ 0 & u^{1} & 0 & 0 \\ \alpha\sigma & 0 & u^{1} & 0 \\ 0 & 0 & 0 & u^{1} \end{pmatrix}, \qquad \mathbf{F}^{2}(\mathbf{q}) = \begin{pmatrix} u^{2} & 0 & 0 & 0 \\ 0 & u^{2} & \alpha\sigma & \frac{-\alpha\sigma^{2}}{4\alpha+2} \\ 0 & \alpha\sigma & u^{2} & 0 \\ 0 & 0 & 0 & u^{2} \end{pmatrix}. \tag{2.4}$$

We shall use the *mathring notation* for gradients. We define the gradient of q by

$$\mathring{\mathbf{q}} := \nabla q \tag{2.5}$$

In the usual orthonormal basis  $(e_1, e_2)$ ,  $\mathring{\mathbf{q}}$  is a  $4 \times 2$ -matrix with components given by  $\mathring{q}_i^j = \partial_i q^j$ ,  $i \in \{1, 2\}$ ,  $j \in \{1, 2, 3, 4\}$ . Letting the gradient operator act upon (2.3), we find that

$$\partial_t \mathring{\mathbf{q}} + \mathbf{F}^i \partial_i \mathring{\mathbf{q}} + \mathring{\mathbf{q}}^j \frac{\partial \mathbf{F}^i}{\partial q^j} \mathring{\mathbf{q}}_i = 0.$$
 (2.6)

Associated to each state vector q and each unit vector n are three distinct wave speeds

$$\lambda_1(q, n) = u \cdot n - \alpha \sigma,$$
  $\lambda_2(q, n) = u \cdot n,$   $\lambda_3(q, n) = u \cdot n + \alpha \sigma,$  (2.7)

which are the eigenvalues of the matrix

$$\mathbf{F}^{n} := \sum_{i=1}^{2} n^{i} \mathbf{F}^{i} = \begin{pmatrix} \boldsymbol{u} \cdot \boldsymbol{n} & 0 & \alpha \sigma n^{1} & \frac{-\alpha \sigma^{2}}{4\alpha + 2} n^{1} \\ 0 & \boldsymbol{u} \cdot \boldsymbol{n} & \alpha \sigma n^{2} & \frac{-\alpha \sigma^{2}}{4\alpha + 2} n^{2} \\ \alpha \sigma n^{1} & \alpha \sigma n^{2} & \boldsymbol{u} \cdot \boldsymbol{n} & 0 \\ 0 & 0 & 0 & \boldsymbol{u} \cdot \boldsymbol{n} \end{pmatrix} . \tag{2.8}$$

Since  $\sigma > 0$ , it follows that  $\lambda_1 < \lambda_2 < \lambda_3$ . The eigenvalue  $\lambda_2$  has multiplicity 2. Corresponding to the three wave speeds in (2.7), we define the three transport velocities

$$\mathbf{v}_1 = \mathbf{u} - \alpha \sigma \mathbf{n}, \qquad \mathbf{v}_2 = \mathbf{u}, \qquad \mathbf{v}_3 = \mathbf{u} + \alpha \sigma \mathbf{n}.$$
 (2.9)

To the unit vector field  $\mathbf{n}(\mathbf{y},t) = n^i(\mathbf{y},t)\mathbf{e}_i$ , we associate its perpendicular vector field

$$\tau(y,t) := n(y,t)^{\perp} = -n^2(y,t)e_1 + n^1(y,t)e_2.$$

The orthonormal frame  $(n, \tau)$  will ultimately play a fundamental geometric role as the unit normal and tangent vector fields, respectively, to the evolving fast acoustic characteristic surfaces. At this stage, it is only important that n and  $\tau$  are orthogonal and of unit length. We introduce the following notation for the components of  $\mathring{\mathbf{q}}$  in the basis  $(n, \tau)$ :

$$\mathring{q}_n := n^i q_{,i} , \qquad \mathring{q}_\tau := \tau^i q_{,i} . \qquad (2.10)$$

The vector equations (2.3) and (2.6) then take the equivalent form

$$\partial_t \mathbf{q} + \mathbf{F}^n(\mathbf{q}) \mathring{\mathbf{q}}_n + \mathbf{F}^{\tau}(\mathbf{q}) \mathring{\mathbf{q}}_{\tau} = 0, \qquad (2.11a)$$

$$\partial_t \mathring{\mathbf{q}} + \mathbf{F}^n(\mathbf{q}) \partial_n \mathring{\mathbf{q}} + \mathbf{F}^\tau(\mathbf{q}) \partial_\tau \mathring{\mathbf{q}} = -\mathring{\mathbf{q}}^j \frac{\partial \mathbf{F}^i}{\partial q^j} \mathring{\mathbf{q}}_i, \tag{2.11b}$$

where  $\mathbf{F}^{\tau} := \sum_{i=1}^{2} \tau^{i} \mathbf{F}^{i}$  and  $\mathring{q}^{j} := (q, 1, q, 2)$ . The summation on the right side of (2.11b) can use either the basis  $(\mathbf{e}_{1}, \mathbf{e}_{2})$  or the basis  $\{\mathbf{n}, \boldsymbol{\tau}\}$ .

2.3. Classical and differentiated Riemann variables. We form the matrix C of left eigenvectors of the matrix  $F^n$  in (2.8):

$$\mathbf{C} = \begin{pmatrix} n^1 & n^2 & -1 & \frac{\sigma}{4\alpha + 2} \\ \tau^1 & \tau^2 & 0 & 0 \\ n^1 & n^2 & 1 & \frac{-\sigma}{4\alpha + 2} \\ 0 & 0 & 0 & 1 \end{pmatrix} . \tag{2.12}$$

Then, we define the  $4 \times 2$ -matrix of differentiated Riemann variables,

$$\mathring{\mathbf{w}} = \mathbf{C}\mathring{\mathbf{q}}. \tag{2.13}$$

In order to follow the notation of [8], we introduce a specific naming convention for the components of  $\mathbf{\mathring{w}}$  as follows:

$$\mathbf{\mathring{w}} = \begin{pmatrix} \mathring{z}_1 & \mathring{z}_2 \\ \mathring{a}_1 & \mathring{a}_2 \\ \mathring{w}_1 & \mathring{w}_2 \\ \mathring{s}_1 & \mathring{s}_2 \end{pmatrix}, \begin{pmatrix} \mathring{z}_n \\ \mathring{a}_n \\ \mathring{w}_n \\ \mathring{s}_n \end{pmatrix} = \begin{pmatrix} \mathring{z}_i n^i \\ \mathring{a}_i n^i \\ \mathring{w}_i n^i \\ \mathring{s}_i n^i \end{pmatrix}, \begin{pmatrix} \mathring{z}_{\tau} \\ \mathring{a}_{\tau} \\ \mathring{w}_{\tau} \\ \mathring{s}_{\tau} \end{pmatrix} = \begin{pmatrix} \mathring{z}_i \tau^i \\ \mathring{a}_i \tau^i \\ \mathring{w}_i \tau^i \\ \mathring{s}_i \tau^i \end{pmatrix}.$$
(2.14)

With the components of the classical Riemann variables defined in (2.14), using the definition of C in (2.12), and the definition (2.13), we obtain that

$$\dot{w}_n = \partial_n \mathbf{u} \cdot \mathbf{n} + \partial_n \sigma - \frac{\sigma}{4\alpha + 2} \partial_n s, \qquad \dot{w}_\tau = \partial_\tau \mathbf{u} \cdot \mathbf{n} + \partial_\tau \sigma - \frac{\sigma}{4\alpha + 2} \partial_\tau s, \qquad (2.15a)$$

$$\dot{z}_n = \partial_n \mathbf{u} \cdot \mathbf{n} - \partial_n \sigma + \frac{\sigma}{4\alpha + 2} \partial_n s, \qquad \dot{z}_\tau = \partial_\tau \mathbf{u} \cdot \mathbf{n} - \partial_\tau \sigma + \frac{\sigma}{4\alpha + 2} \partial_\tau s, \qquad (2.15b)$$

$$\mathring{a}_n = \partial_n \mathbf{u} \cdot \mathbf{\tau}, \qquad \qquad \mathring{a}_{\tau} = \partial_{\tau} \mathbf{u} \cdot \mathbf{\tau}, \qquad (2.15c)$$

$$\mathring{s}_n = \partial_n s, \qquad \qquad \mathring{s}_\tau = \partial_\tau s. \tag{2.15d}$$

Moreover, a short computation shows that (2.15) can be written as

$$\mathring{w}_n = \partial_n w + a \partial_n \tau \cdot \mathbf{n}, \qquad \mathring{w}_\tau = \partial_\tau w + a \partial_\tau \tau \cdot \mathbf{n}, \qquad (2.16a)$$

$$\dot{z}_n = \partial_n z + a \partial_n \boldsymbol{\tau} \cdot \boldsymbol{n}, \qquad \dot{z}_\tau = \partial_\tau z + a \partial_\tau \boldsymbol{\tau} \cdot \boldsymbol{n}, \qquad (2.16b)$$

$$\mathring{a}_n = \partial_n a - \frac{1}{2}(w+z)\partial_n \boldsymbol{\tau} \cdot \boldsymbol{n}, \qquad \mathring{a}_\tau = \partial_\tau a - \frac{1}{2}(w+z)\partial_\tau \boldsymbol{\tau} \cdot \boldsymbol{n}. \qquad (2.16c)$$

The normal and tangential derivatives of  $\sigma$  can be recovered as

$$\partial_n \sigma = \frac{1}{2} (\mathring{w}_n - \mathring{z}_n) + \frac{\sigma}{4\alpha + 2} \mathring{s}_n, \qquad \partial_\tau \sigma = \frac{1}{2} (\mathring{w}_\tau - \mathring{z}_\tau) + \frac{\sigma}{4\alpha + 2} \mathring{s}_\tau.$$

Similarly, the compression and vorticity of the flow is given by

$$\operatorname{div} \mathbf{u} = \frac{1}{2}(\mathring{w}_n + \mathring{z}_n) + \mathring{a}_{\tau}, \qquad \operatorname{curl} \mathbf{u} = \mathring{a}_n - \frac{1}{2}(\mathring{w}_{\tau} + \mathring{z}_{\tau}). \tag{2.17}$$

We also define the classical Riemann variables

$$w = u \cdot n + \sigma,$$
  $z = u \cdot n - \sigma,$   $a = u \cdot \tau.$  (2.18)

From (2.18), we see that the velocity u and rescaled sound speed  $\sigma$  can be obtained from w, z, and a via the relations

$$\mathbf{u} = \frac{1}{2}(w+z)\mathbf{n} + a\mathbf{\tau}, \qquad \qquad \sigma = \frac{1}{2}(w-z). \tag{2.19}$$

# 2.4. The Euler equations in terms of Riemann variables. We define the matrices

$$\mathbf{E}^n := \mathbf{C}\mathbf{F}^n\mathbf{C}^{-1} = \operatorname{diag}(\lambda_1, \lambda_2, \lambda_3, \lambda_2), \tag{2.20a}$$

and

$$\mathbf{E}^{\tau} := \mathbf{C}\mathbf{F}^{\tau}\mathbf{C}^{-1} = \begin{pmatrix} \boldsymbol{u} \cdot \boldsymbol{\tau} & -\alpha\sigma & 0 & 0\\ \frac{1}{2}\alpha\sigma & \boldsymbol{u} \cdot \boldsymbol{\tau} & -\frac{1}{2}\alpha\sigma & 0\\ 0 & \alpha\sigma & \boldsymbol{u} \cdot \boldsymbol{\tau} & 0\\ 0 & 0 & 0 & \boldsymbol{u} \cdot \boldsymbol{\tau} \end{pmatrix},$$
(2.20b)

where  $\lambda_1$ ,  $\lambda_2$ , and  $\lambda_3$  are defined in (2.7). Multiplying equation (2.11b) on the left by C, we find that

$$\mathbf{C}\partial_t \mathring{\mathbf{q}} + \mathbf{E}^n \mathbf{C}\partial_n \mathring{\mathbf{q}} + \mathbf{E}^\tau \mathbf{C}\partial_\tau \mathring{\mathbf{q}} = -\mathbf{C} \left( \mathring{q}^j \frac{\partial \mathbf{F}^i}{\partial q^j} \mathring{q}_i \right). \tag{2.21a}$$

Commutation of C about the partial derivatives in (2.21) yields

$$\partial_t \mathring{\mathbf{w}} + \mathbf{E}^n \partial_n \mathring{\mathbf{w}} + \mathbf{E}^\tau \partial_\tau \mathring{\mathbf{w}} = (\partial_t \mathbf{C} + \mathbf{E}^n \partial_n \mathbf{C} + \mathbf{E}^\tau \partial_\tau \mathbf{C}) \mathbf{C}^{-1} \mathring{\mathbf{w}} - \mathbf{C} \left( \mathring{\mathbf{q}}^j \frac{\partial \mathbf{F}^i}{\partial q^j} \mathbf{C}^{-1} \mathring{\mathbf{w}}_i \right). \tag{2.22}$$

By computing the inner-product of (2.22) with the vector fields n and  $\tau$ , we obtain that

$$\partial_t \mathring{\mathbf{w}}_n + \mathbf{E}^n \partial_n \mathring{\mathbf{w}}_n + \mathbf{E}^\tau \partial_\tau \mathring{\mathbf{w}}_n = \mathring{\mathbf{g}}_n, \tag{2.23a}$$

$$\partial_t \mathring{\boldsymbol{w}}_{\tau} + \mathbf{E}^n \partial_n \mathring{\boldsymbol{w}}_{\tau} + \mathbf{E}^{\tau} \partial_{\tau} \mathring{\boldsymbol{w}}_{\tau} = \mathring{\boldsymbol{g}}_{\tau} , \qquad (2.23b)$$

where

$$\mathring{g}_{n} = \underbrace{(\partial_{t} \boldsymbol{n} \cdot \boldsymbol{\tau} + (\partial_{n} \boldsymbol{n} \cdot \boldsymbol{\tau}) \mathbf{E}^{n} + (\partial_{\tau} \boldsymbol{n} \cdot \boldsymbol{\tau}) \mathbf{E}^{\tau})}_{-\mathbf{P}_{1}} \mathring{\boldsymbol{w}}_{\tau} + \underbrace{(\partial_{t} \mathbf{C} + \mathbf{E}^{n} \partial_{n} \mathbf{C} + \mathbf{E}^{\tau} \partial_{\tau} \mathbf{C}) \mathbf{C}^{-1}}_{\mathbf{P}_{2}} \mathring{\boldsymbol{w}}_{n} - \underbrace{\mathring{q}_{n}^{j} \mathbf{C} \frac{\partial \mathbf{F}^{n}}{\partial q^{j}} \mathbf{C}^{-1}}_{\mathbf{P}_{n}^{n}} \mathring{\boldsymbol{w}}_{n} - \underbrace{\mathring{q}_{n}^{j} \mathbf{C} \frac{\partial \mathbf{F}^{\tau}}{\partial q^{j}} \mathbf{C}^{-1}}_{\mathbf{P}_{n}^{\tau}} \mathring{\boldsymbol{w}}_{\tau}, \tag{2.24a}$$

$$\mathring{g}_{\tau} = \underbrace{(\partial_{t}\boldsymbol{\tau} \cdot \boldsymbol{n} + (\partial_{n}\boldsymbol{\tau} \cdot \boldsymbol{n})\mathbf{E}^{n} + (\partial_{\tau}\boldsymbol{\tau} \cdot \boldsymbol{n})\mathbf{E}^{\tau})}_{\mathbf{P}_{1}} \mathring{\boldsymbol{w}}_{n} + \underbrace{(\partial_{t}\mathbf{C} + \mathbf{E}^{n}\partial_{n}\mathbf{C} + \mathbf{E}^{\tau}\partial_{\tau}\mathbf{C})\mathbf{C}^{-1}}_{\mathbf{P}_{2}} \mathring{\boldsymbol{w}}_{\tau} - \underbrace{\mathring{q}_{\tau}^{j}\mathbf{C}\frac{\partial\mathbf{F}^{n}}{\partial q^{j}}\mathbf{C}^{-1}}_{\mathbf{P}^{\tau}} \mathring{\boldsymbol{w}}_{n} - \underbrace{\mathring{q}_{\tau}^{j}\mathbf{C}\frac{\partial\mathbf{F}^{\tau}}{\partial q^{j}}\mathbf{C}^{-1}}_{\mathbf{P}^{\tau}} \mathring{\boldsymbol{w}}_{\tau}.$$
(2.24b)

It is notationally convenient for us to introduce the following *spacetime curvature components*, which appear in (2.24) and in many other computed Eulerian relations:

$$\kappa_t = (\partial_t + \mathbf{v}_3 \cdot \nabla) \mathbf{\tau} \cdot \mathbf{n}, \qquad \kappa_n = \partial_n \mathbf{\tau} \cdot \mathbf{n}, \qquad \kappa_\tau = \partial_\tau \mathbf{\tau} \cdot \mathbf{n}. \qquad (2.25)$$

We note that

$$(\partial_t + \boldsymbol{v}_i \cdot \boldsymbol{\nabla})\boldsymbol{\tau} \cdot \boldsymbol{n} = \kappa_t + (i-3)\kappa_n,$$
  $i = 1, 2, 3.$ 

The matrices  $P_1$ ,  $P_2$  which appear in (2.24) simplify as follows:

$$\mathbf{P}_{1} = \kappa_{t} \mathbf{I} + \kappa_{n} (\mathbf{E}^{n} - \lambda_{3} \mathbf{I}) + \kappa_{\tau} (\mathbf{E}^{\tau} - a \mathbf{I}) 
= \begin{pmatrix} \kappa_{t} - 2\alpha\sigma\kappa_{n} & -\alpha\sigma\kappa_{\tau} & 0 & 0 \\ \frac{1}{2}\alpha\sigma\kappa_{\tau} & \kappa_{t} - \alpha\sigma\kappa_{n} & -\frac{1}{2}\alpha\sigma\kappa_{\tau} & 0 \\ 0 & \alpha\sigma\kappa_{\tau} & \kappa_{t} & 0 \\ 0 & 0 & 0 & \kappa_{t} - \alpha\sigma\kappa_{n} \end{pmatrix},$$

$$\mathbf{P}_{2} = ((\partial_{t} + \mathbf{v}_{2} \cdot \mathbf{\nabla})\mathbf{C} + (\mathbf{E}^{n} - \lambda_{2}\mathbf{I})\partial_{n}\mathbf{C} + (\mathbf{E}^{\tau} - a\mathbf{I})\partial_{\sigma}\mathbf{C})\mathbf{C}^{-1}$$
(2.26a)

$$= \begin{pmatrix} -\frac{1}{2}\alpha\sigma\kappa_{\tau} & -\kappa_{t} + 2\alpha\sigma\kappa_{n} & -\frac{1}{2}\alpha\sigma\kappa_{\tau} & \frac{-\alpha\sigma}{4\alpha+2}(\operatorname{div}u + \partial_{n}\sigma) \\ \frac{1}{2}(\kappa_{t} - \alpha\sigma\kappa_{n}) & 0 & \frac{1}{2}(\kappa_{t} - \alpha\sigma\kappa_{n}) & \frac{-\alpha\sigma}{4\alpha+2}\partial_{\tau}\sigma \\ \frac{1}{2}\alpha\sigma\kappa_{\tau} & -\kappa_{t} & \frac{1}{2}\alpha\sigma\kappa_{\tau} & \frac{-\alpha\sigma}{4\alpha+2}(\operatorname{div}u - \partial_{n}\sigma) \\ 0 & 0 & 0 & 0 \end{pmatrix},$$
(2.26b)

Using the chain rule, we compute that

$$\mathbf{P}_{\mu}^{n} = \begin{pmatrix} \partial_{\mu} \boldsymbol{u} \cdot \boldsymbol{n} - \alpha \partial_{\mu} \sigma & 0 & 0 & \frac{-\alpha \sigma}{4\alpha + 2} \partial_{\mu} \sigma \\ 0 & \partial_{\mu} \boldsymbol{u} \cdot \boldsymbol{n} & 0 & 0 \\ 0 & 0 & \partial_{\mu} \boldsymbol{u} \cdot \boldsymbol{n} + \alpha \partial_{\mu} \sigma & \frac{\alpha \sigma}{4\alpha + 2} \partial_{\mu} \sigma \\ 0 & 0 & 0 & 0 & \partial_{\mu} \boldsymbol{u} \cdot \boldsymbol{n} \end{pmatrix} \text{ for } \mu \in \{n, \tau\},$$

$$\mathbf{P}_{\mu}^{\tau} = \begin{pmatrix} \partial_{\mu} \boldsymbol{u} \cdot \boldsymbol{\tau} - \alpha \partial_{\mu} \sigma & -\alpha \partial_{\mu} \sigma & 0 & 0 \\ \frac{1}{2} \alpha \partial_{\mu} \sigma & \partial_{\mu} \boldsymbol{u} \cdot \boldsymbol{\tau} & -\frac{1}{2} \alpha \partial_{\mu} \sigma & \frac{-\alpha \sigma}{4\alpha + 2} \partial_{\mu} \sigma \\ 0 & \alpha \partial_{\mu} \sigma & \partial_{\mu} \boldsymbol{u} \cdot \boldsymbol{\tau} + \alpha \partial_{\mu} \sigma & 0 \\ 0 & 0 & 0 & \partial_{\mu} \boldsymbol{u} \cdot \boldsymbol{\tau} \end{pmatrix} \text{ for } \mu \in \{n, \tau\}.$$

$$(2.27a)$$

$$\mathbf{P}_{\mu}^{\tau} = \begin{pmatrix} \partial_{\mu} \boldsymbol{u} \cdot \boldsymbol{\tau} - \alpha \partial_{\mu} \sigma & -\alpha \partial_{\mu} \sigma & 0 & 0\\ \frac{1}{2} \alpha \partial_{\mu} \sigma & \partial_{\mu} \boldsymbol{u} \cdot \boldsymbol{\tau} & -\frac{1}{2} \alpha \partial_{\mu} \sigma & \frac{-\alpha \sigma}{4\alpha + 2} \partial_{\mu} \sigma\\ 0 & \alpha \partial_{\mu} \sigma & \partial_{\mu} \boldsymbol{u} \cdot \boldsymbol{\tau} + \alpha \partial_{\mu} \sigma & 0\\ 0 & 0 & 0 & \partial_{\mu} \boldsymbol{u} \cdot \boldsymbol{\tau} \end{pmatrix} \text{ for } \mu \in \{n, \tau\}.$$
 (2.27b)

$$(\partial_{t} + \boldsymbol{v}_{3} \cdot \boldsymbol{\nabla})\mathring{w}_{n} + \alpha\sigma\partial_{\tau}\mathring{a}_{n} = -(\mathring{w}_{\tau} + \mathring{a}_{n})(\partial_{t} + \boldsymbol{v}_{3} \cdot \boldsymbol{\nabla})\boldsymbol{\tau} \cdot \boldsymbol{n} + \alpha\sigma(\frac{1}{2}(\mathring{w}_{n} + \mathring{z}_{n}) - \mathring{a}_{\tau})\partial_{\tau}\boldsymbol{\tau} \cdot \boldsymbol{n}$$

$$-(\frac{1+\alpha}{2}\mathring{w}_{n} + \frac{1-\alpha}{2}\mathring{z}_{n} + \frac{\alpha\sigma}{4\alpha+2}\mathring{s}_{n})\mathring{w}_{n} - \frac{\alpha\sigma}{4\alpha+2}(\frac{1}{2}(\mathring{w}_{n} + \mathring{z}_{n}) + \mathring{a}_{\tau})\mathring{s}_{n}$$

$$-\mathring{a}_{n}\mathring{w}_{\tau} - (\mathring{w}_{\tau} + \mathring{a}_{\tau})(\frac{\alpha}{2}(\mathring{w}_{n} - \mathring{z}_{n}) + \frac{\alpha\sigma}{4\alpha+2}\mathring{s}_{n}),$$

$$(2.28a)$$

$$(\partial_{t} + \boldsymbol{v}_{1} \cdot \boldsymbol{\nabla}) \mathring{z}_{n} - \alpha \sigma \partial_{\tau} \mathring{a}_{n} = -(\mathring{z}_{\tau} + \mathring{a}_{n})(\partial_{t} + \boldsymbol{v}_{1} \cdot \boldsymbol{\nabla})\boldsymbol{\tau} \cdot \boldsymbol{n} - \alpha \sigma(\frac{1}{2}(\mathring{w}_{n} + \mathring{z}_{n}) - \mathring{a}_{\tau})\partial_{\tau}\boldsymbol{\tau} \cdot \boldsymbol{n}$$

$$-(\frac{1-\alpha}{2}\mathring{w}_{n} + \frac{1+\alpha}{2}\mathring{z}_{n} - \frac{\alpha\sigma}{4\alpha+2}\mathring{s}_{n})\mathring{z}_{n} - \frac{\alpha\sigma}{4\alpha+2}(\frac{1}{2}(\mathring{w}_{n} + \mathring{z}_{n}) + \mathring{a}_{\tau})\mathring{s}_{n}$$

$$-\mathring{a}_{n}\mathring{z}_{\tau} + (\mathring{z}_{\tau} + \mathring{a}_{\tau})(\frac{\alpha}{2}(\mathring{w}_{n} - \mathring{z}_{n}) + \frac{\alpha\sigma}{4\alpha+2}\mathring{s}_{n}),$$

$$(2.28b)$$

$$(\partial_{t} + \boldsymbol{v}_{2} \cdot \boldsymbol{\nabla})\mathring{a}_{n} + \frac{\alpha}{2}\sigma\partial_{\tau}(\mathring{w}_{n} - \mathring{z}_{n}) = (\frac{1}{2}(\mathring{w}_{n} + \mathring{z}_{n}) - \mathring{a}_{\tau})(\partial_{t} + \boldsymbol{v}_{2} \cdot \boldsymbol{\nabla})\boldsymbol{\tau} \cdot \boldsymbol{n}$$

$$+ \frac{\alpha}{2}\sigma(\mathring{w}_{\tau} + \mathring{z}_{\tau})\partial_{\tau}\boldsymbol{\tau} \cdot \boldsymbol{n} - \frac{\alpha\sigma}{4\alpha+2}(\frac{1}{2}(\mathring{w}_{\tau} - \mathring{z}_{\tau}) + \frac{\sigma}{4\alpha+2}\mathring{s}_{\tau})\mathring{s}_{n} - \frac{1}{2}(\mathring{w}_{n} + \mathring{z}_{n})\mathring{a}_{n}$$

$$+ \alpha(\frac{1}{2}(\mathring{w}_{\tau} - \mathring{z}_{\tau}) + \frac{\sigma}{4\alpha+2}\mathring{s}_{\tau})(\frac{1}{2}(\mathring{w}_{n} - \mathring{z}_{n}) + \frac{\sigma}{4\alpha+2}\mathring{s}_{n}),$$

$$(2.28c)$$

$$(\partial_t + \boldsymbol{v}_2 \cdot \boldsymbol{\nabla}) \mathring{\boldsymbol{s}}_n = -\mathring{\boldsymbol{s}}_\tau (\partial_t + \boldsymbol{v}_2 \cdot \boldsymbol{\nabla}) \boldsymbol{\tau} \cdot \boldsymbol{n} - \frac{1}{2} (\mathring{\boldsymbol{w}}_n + \mathring{\boldsymbol{z}}_n) \mathring{\boldsymbol{s}}_n - \mathring{\boldsymbol{a}}_n \mathring{\boldsymbol{s}}_\tau , \tag{2.28d}$$

$$(\partial_{t} + \boldsymbol{v}_{3} \cdot \boldsymbol{\nabla})\mathring{w}_{\tau} + \alpha\sigma\partial_{\tau}\mathring{a}_{\tau} = (\mathring{w}_{n} - \mathring{a}_{\tau})(\partial_{t} + \boldsymbol{v}_{3} \cdot \boldsymbol{\nabla})\boldsymbol{\tau} \cdot \boldsymbol{n} + \alpha\sigma(\frac{1}{2}(\mathring{w}_{\tau} + \mathring{z}_{\tau}) + \mathring{a}_{n})\partial_{\tau}\boldsymbol{\tau} \cdot \boldsymbol{n}$$

$$- (\frac{1+\alpha}{2}\mathring{w}_{\tau} + \frac{1-\alpha}{2}\mathring{z}_{\tau} + \frac{\alpha\sigma}{4\alpha+2}\mathring{s}_{\tau})\mathring{w}_{n} - \frac{\alpha\sigma}{4\alpha+2}(\frac{1}{2}(\mathring{w}_{\tau} - \mathring{z}_{\tau}) + \frac{\sigma}{4\alpha+2}\mathring{s}_{\tau})\mathring{s}_{n}$$

$$- \mathring{w}_{\tau}\mathring{a}_{\tau} - (\mathring{w}_{\tau} + \mathring{a}_{\tau})(\frac{\alpha}{2}(\mathring{w}_{\tau} - \mathring{z}_{\tau}) + \frac{\sigma}{4\alpha+2}\mathring{s}_{\tau}),$$

$$(2.28e)$$

$$(\partial_{t} + \boldsymbol{v}_{1} \cdot \boldsymbol{\nabla})\mathring{z}_{\tau} - \alpha\sigma\partial_{\tau}\mathring{a}_{\tau} = (\mathring{z}_{n} - \mathring{a}_{\tau})(\partial_{t} + \boldsymbol{v}_{1} \cdot \boldsymbol{\nabla})\boldsymbol{\tau} \cdot \boldsymbol{n} - \alpha\sigma(\frac{1}{2}(\mathring{w}_{\tau} + \mathring{z}_{\tau}) + \mathring{a}_{\tau})\partial_{\tau}\boldsymbol{\tau} \cdot \boldsymbol{n}$$

$$- (\frac{1-\alpha}{2}\mathring{w}_{\tau} + \frac{1+\alpha}{2}\mathring{z}_{\tau} - \frac{\alpha\sigma}{4\alpha+2}\mathring{s}_{\tau})\mathring{z}_{n} + \frac{\alpha\sigma}{4\alpha+2}(\frac{1}{2}(\mathring{w}_{\tau} - \mathring{z}_{\tau}) + \frac{\sigma}{4\alpha+2}\mathring{s}_{\tau})\mathring{s}_{n}$$

$$- \mathring{z}_{\tau}\mathring{a}_{\tau} + (\mathring{z}_{\tau} + \mathring{a}_{\tau})(\frac{\alpha}{2}(\mathring{w}_{\tau} - \mathring{z}_{\tau}) + \frac{\sigma}{4\alpha+2}\mathring{s}_{\tau}),$$

$$(2.28f)$$

$$(\partial_t + \boldsymbol{v}_2 \cdot \boldsymbol{\nabla}) \mathring{a}_{\tau} + \frac{\alpha}{2} \sigma \partial_{\tau} (\mathring{w}_{\tau} - \mathring{z}_{\tau}) = (\frac{1}{2} (\mathring{w}_{\tau} + \mathring{z}_{\tau}) + \mathring{a}_n) (\partial_t + \boldsymbol{v}_2 \cdot \boldsymbol{\nabla}) \boldsymbol{\tau} \cdot \boldsymbol{n} - \frac{\alpha}{2} \sigma (\mathring{w}_n - \mathring{z}_n) \partial_{\tau} \boldsymbol{\tau} \cdot \boldsymbol{n} - \frac{1}{2} (\mathring{w}_{\tau} + \mathring{z}_{\tau}) \mathring{a}_n - \mathring{a}_{\tau}^2 + \alpha (\frac{1}{2} (\mathring{w}_{\tau} + \mathring{z}_{\tau}) + \frac{\sigma}{4\alpha + 2} \mathring{s}_{\tau})^2,$$

$$(2.28g)$$

$$(\partial_t + \boldsymbol{v}_2 \cdot \boldsymbol{\nabla}) \mathring{\boldsymbol{s}}_{\tau} = \mathring{\boldsymbol{s}}_n (\partial_t + \boldsymbol{v}_2 \cdot \boldsymbol{\nabla}) \boldsymbol{\tau} \cdot \boldsymbol{n} - \frac{1}{2} (\mathring{\boldsymbol{w}}_{\tau} + \mathring{\boldsymbol{z}}_{\tau}) \mathring{\boldsymbol{s}}_n - \mathring{\boldsymbol{a}}_{\tau} \mathring{\boldsymbol{s}}_{\tau} . \tag{2.28h}$$

In addition, the classical Riemann variables (2.18) satisfy

$$(\partial_t + \boldsymbol{v}_3 \cdot \boldsymbol{\nabla})w + \alpha \sigma \mathring{a}_{\tau} - \frac{\alpha \sigma^2}{4\alpha + 2} \mathring{s}_n = -a(\partial_t + \boldsymbol{v}_3 \cdot \boldsymbol{\nabla})\boldsymbol{\tau} \cdot \boldsymbol{n}, \qquad (2.29a)$$

$$(\partial_t + \boldsymbol{v}_1 \cdot \nabla)z - \alpha \sigma \mathring{a}_\tau + \frac{\alpha \sigma^2}{4\alpha + 2} \mathring{s}_n = -a(\partial_t + \boldsymbol{v}_1 \cdot \nabla)\boldsymbol{\tau} \cdot \boldsymbol{n}, \qquad (2.29b)$$

$$(\partial_t + \boldsymbol{v}_2 \cdot \boldsymbol{\nabla})a + \frac{\alpha}{2}\sigma(\mathring{w}_{\tau} - \mathring{z}_{\tau}) = \frac{1}{2}(w+z)(\partial_t + \boldsymbol{v}_2 \cdot \boldsymbol{\nabla})\boldsymbol{\tau} \cdot \boldsymbol{n}, \qquad (2.29c)$$

$$(\partial_t + \mathbf{v}_2 \cdot \nabla) s = 0. \tag{2.29d}$$

Using the formulas (2.26)–(2.27), the identities (2.24), and

$$\mathring{\sigma}_n := \partial_n \sigma = \tfrac{1}{2} (\mathring{w}_n - \mathring{z}_n) + \tfrac{\sigma}{4\alpha + 2} \mathring{s}_n \,, \ \ \mathring{\sigma}_\tau := \partial_\tau \sigma = \tfrac{1}{2} (\mathring{w}_\tau - \mathring{z}_\tau) + \tfrac{\sigma}{4\alpha + 2} \mathring{s}_\tau \,,$$

we write the equations (2.28)–(2.29) as transport equations along the fast acoustic transport velocity:

$$(\partial_t + \boldsymbol{v}_3 \cdot \boldsymbol{\nabla}) \mathring{\boldsymbol{w}}_n + \alpha \sigma \partial_\tau \mathring{\boldsymbol{a}}_n = -(\mathring{\boldsymbol{w}}_\tau + \mathring{\boldsymbol{a}}_n) \kappa_t + \alpha \sigma (\frac{1}{2} (\mathring{\boldsymbol{w}}_n + \mathring{\boldsymbol{z}}_n) - \mathring{\boldsymbol{a}}_\tau) \kappa_\tau$$

$$-\left(\frac{1+\alpha}{2}\mathring{w}_{n} + \frac{1-\alpha}{2}\mathring{z}_{n} + \frac{\alpha\sigma}{4\alpha+2}\mathring{s}_{n}\right)\mathring{w}_{n} - \frac{\alpha\sigma}{4\alpha+2}\left(\frac{1}{2}(\mathring{w}_{n} + \mathring{z}_{n}) + \mathring{a}_{\tau}\right)\mathring{s}_{n} - \mathring{a}_{n}\mathring{w}_{\tau} - \alpha(\mathring{w}_{\tau} + \mathring{a}_{\tau})\mathring{\sigma}_{n},$$
(2.30a)

$$(\partial_{t} + \mathbf{v}_{3} \cdot \nabla) \mathring{z}_{n} - 2\alpha\sigma\partial_{n}\mathring{z}_{n} - \alpha\sigma\partial_{\tau}\mathring{a}_{n} = -(\mathring{z}_{\tau} + \mathring{a}_{n})(\kappa_{t} - 2\alpha\sigma\kappa_{n}) - \alpha\sigma(\frac{1}{2}(\mathring{w}_{n} + \mathring{z}_{n}) - \mathring{a}_{\tau})\kappa_{\tau}$$

$$- (\frac{1-\alpha}{2}\mathring{w}_{n} + \frac{1+\alpha}{2}\mathring{z}_{n} - \frac{\alpha\sigma}{4\alpha+2}\mathring{s}_{n})\mathring{z}_{n} - \frac{\alpha\sigma}{4\alpha+2}(\frac{1}{2}(\mathring{w}_{n} + \mathring{z}_{n}) + \mathring{a}_{\tau})\mathring{s}_{n}$$

$$- \mathring{a}_{n}\mathring{z}_{\tau} + (\mathring{z}_{\tau} + \mathring{a}_{\tau})\mathring{\sigma}_{n} ,$$
(2.30b)

$$(\partial_t + \boldsymbol{v}_3 \cdot \boldsymbol{\nabla}) \mathring{a}_n - \alpha \sigma \partial_n \mathring{a}_n + \frac{\alpha}{2} \sigma \partial_\tau (\mathring{w}_n - \mathring{z}_n) = (\frac{1}{2} (\mathring{w}_n + \mathring{z}_n) - \mathring{a}_\tau) (\kappa_t - \alpha \sigma \kappa_n) + \frac{\alpha}{2} \sigma (\mathring{w}_\tau + \mathring{z}_\tau) \kappa_\tau - \frac{\alpha \sigma}{4\alpha + 2} \mathring{\sigma}_\tau \mathring{s}_n - \frac{1}{2} (\mathring{w}_n + \mathring{z}_n) \mathring{a}_n + \alpha \mathring{\sigma}_n \mathring{\sigma}_\tau ,$$
(2.30c)

$$(\partial_t + \boldsymbol{v}_3 \cdot \boldsymbol{\nabla}) \mathring{\boldsymbol{s}}_n - \alpha \sigma \partial_n \mathring{\boldsymbol{s}}_n = -\mathring{\boldsymbol{s}}_\tau (\kappa_t - \alpha \sigma \kappa_n) - \frac{1}{2} (\mathring{\boldsymbol{w}}_n + \mathring{\boldsymbol{z}}_n) \mathring{\boldsymbol{s}}_n - \mathring{\boldsymbol{a}}_n \mathring{\boldsymbol{s}}_\tau , \tag{2.30d}$$

$$(\partial_t + \boldsymbol{v}_3 \cdot \boldsymbol{\nabla}) \mathring{w}_{\tau} + \alpha \sigma \partial_{\tau} \mathring{a}_{\tau} = (\mathring{w}_n - \mathring{a}_{\tau}) \kappa_t + \alpha \sigma (\frac{1}{2} (\mathring{w}_{\tau} + \mathring{z}_{\tau}) + \mathring{a}_n) \kappa_{\tau} - (\frac{1+\alpha}{2} \mathring{w}_{\tau} + \frac{1-\alpha}{2} \mathring{z}_{\tau} + \frac{\alpha \sigma}{4\alpha+2} \mathring{s}_{\tau}) \mathring{w}_n - \frac{\alpha \sigma}{4\alpha+2} \mathring{\sigma}_{\tau} \mathring{s}_n - \mathring{w}_{\tau} \mathring{a}_{\tau} - \alpha (\mathring{w}_{\tau} + \mathring{a}_{\tau}) \mathring{\sigma}_{\tau},$$

$$(2.30e)$$

$$(\partial_{t} + \boldsymbol{v}_{3} \cdot \boldsymbol{\nabla}) \mathring{z}_{\tau} - 2\alpha\sigma\partial_{n}\mathring{z}_{\tau} - \alpha\sigma\partial_{\tau}\mathring{a}_{\tau} = (\mathring{z}_{n} - \mathring{a}_{\tau})(\kappa_{t} - 2\alpha\sigma\kappa_{n}) - \alpha\sigma(\frac{1}{2}(\mathring{w}_{\tau} + \mathring{z}_{\tau}) + \mathring{a}_{\tau})\kappa_{\tau} - (\frac{1-\alpha}{2}\mathring{w}_{\tau} + \frac{1+\alpha}{2}\mathring{z}_{\tau} - \frac{\alpha\sigma}{4\alpha+2}\mathring{s}_{\tau})\mathring{z}_{n} + \frac{\alpha\sigma}{4\alpha+2}\mathring{\sigma}_{\tau}\mathring{s}_{n} - \mathring{z}_{\tau}\mathring{a}_{\tau} + \alpha(\mathring{z}_{\tau} + \mathring{a}_{\tau})\mathring{\sigma}_{\tau},$$

$$(2.30f)$$

$$(\partial_t + \boldsymbol{v}_3 \cdot \boldsymbol{\nabla}) \mathring{a}_{\tau} - \alpha \sigma \partial_n \mathring{a}_{\tau} + \frac{\alpha}{2} \sigma \partial_{\tau} (\mathring{w}_{\tau} - \mathring{z}_{\tau}) = (\frac{1}{2} (\mathring{w}_{\tau} + \mathring{z}_{\tau}) + \mathring{a}_n) (\kappa_t - \alpha \sigma \kappa_n) - \frac{\alpha}{2} \sigma (\mathring{w}_n - \mathring{z}_n) \kappa_{\tau} - \frac{1}{2} (\mathring{w}_{\tau} + \mathring{z}_{\tau}) \mathring{a}_n - \mathring{a}_{\tau}^2 + \alpha \mathring{\sigma}_{\tau}^2,$$
(2.30g)

$$(\partial_t + \boldsymbol{v}_3 \cdot \boldsymbol{\nabla}) \mathring{\boldsymbol{s}}_{\tau} - \alpha \sigma \partial_n \mathring{\boldsymbol{s}}_{\tau} = \mathring{\boldsymbol{s}}_n (\kappa_t - \alpha \sigma \kappa_n) - \frac{1}{2} (\mathring{\boldsymbol{w}}_{\tau} + \mathring{\boldsymbol{z}}_{\tau}) \mathring{\boldsymbol{s}}_n - \mathring{\boldsymbol{a}}_{\tau} \mathring{\boldsymbol{s}}_{\tau}. \tag{2.30h}$$

and

$$(\partial_t + \boldsymbol{v}_3 \cdot \boldsymbol{\nabla})w + \alpha \sigma \mathring{a}_\tau - \frac{\alpha \sigma^2}{4\alpha + 2} \mathring{s}_n = -a\kappa_t, \qquad (2.31a)$$

$$(\partial_t + \boldsymbol{v}_3 \cdot \boldsymbol{\nabla})z - 2\alpha\sigma \mathring{z}_n - \alpha\sigma \mathring{a}_\tau + \frac{\alpha\sigma^2}{4\alpha + 2}\mathring{s}_n = -a\kappa_t, \qquad (2.31b)$$

$$(\partial_t + \boldsymbol{v}_3 \cdot \nabla)a - \alpha \sigma \mathring{a}_n + \frac{\alpha}{2} \sigma (\mathring{w}_\tau - \mathring{z}_\tau) = \frac{1}{2} (w + z) \kappa_t, \qquad (2.31c)$$

$$(\partial_t + \mathbf{v}_3 \cdot \nabla)s - \alpha \sigma \mathring{s}_n = 0. \tag{2.31d}$$

2.5. Initial conditions for shock formation. We shall now provide a description of the initial conditions to be used for shock formation at the initial time-slice  $\{t=\mathsf{t}_{\mathsf{in}}\}$ . We refer the reader to Section 4.2 of [8] for precise technical assumptions that are needed in order for the rigorous analysis of the  $\overline{\mathsf{MGHD}}$ . For computational shock formation we work with the class of initial data given in Definition 2.1 below. Here, it is convenient to state assumptions in terms of the variables Riemann-type  $(w_0, z_0, a_0, s_0)$ , where  $(w_0, z_0, a_0)$  are defined as in (2.18) with  $n = \mathsf{e}_1, \tau = \mathsf{e}_2$  (this choice of initial normal and tangent vector is made without loss of generality, as the Euler system is rotationally invariant).

**Definition 2.1** (Generic and compressive initial data prescribed on  $\{t=\mathsf{t}_{\mathsf{in}}\}$ ). The  $C^4(\mathbb{T}^2)$  functions  $(w_0,z_0,a_0,s_0)$  are called generic and compressive if there exist parameters  $\kappa_0 \geq 2$  and  $0 < \varepsilon \leq \frac{1}{2}$  such that the following hold:

(1) The data is bounded away from vacuum, and this distance is quantified in terms of  $\kappa_0$ . *Precisely, the initial sound speed is assumed to satisfy the bound* 

$$2\sigma_0(\boldsymbol{x}) = w_0(\boldsymbol{x}) - z_0(\boldsymbol{x}) \ge \frac{1}{2}\kappa_0, \quad \forall \boldsymbol{x} \in \mathbb{T}^2.$$

(2) The gradient of the dominant Riemann-variable  $w_0$  attains a negative non-dengenerate global minimum. That is, at this global minimum (which by translation symmetry may be assumed to hold at x = 0) we assume that the second-derivative test holds, and that without loss of generality (taking into account the rotational symmetry) the derivative of  $w_0$  in the direction of  $x_2$  is smaller than the derivative in the direction of  $x_1$ ; we denote the ratio of these two derivatives by  $\varepsilon$ . Precisely, we assume that

$$-\frac{1}{\varepsilon} := \partial_1 w_0(0) < \partial_1 w_0(\boldsymbol{x}), \ \forall \boldsymbol{x} \in \mathbb{T}^2 \setminus \{0\}, \qquad \nabla^2 \partial_1 w_0(0) \ge \frac{1}{\varepsilon^3} \mathrm{Id}, \qquad |\partial_2 w_0(\boldsymbol{x})| \le 1, \ \forall \boldsymbol{x} \in \mathbb{T}^2.$$

(3) For each fixed  $x_2 \in \mathbb{T}$ , the function  $\partial_1 w_0(\cdot, x_2)$  attains a non-degenerate global minimum at some  $x_1^{\vee} \in \mathbb{T}$ . Precisely, we assume that for each  $x_2 \in \mathbb{T}$ , there exists  $x_1^{\vee} = x_1^{\vee}(x_2) \in \mathbb{T}$  such that  $\partial_1 w_0(x_1^{\vee}(x_2), x_2) < 0$   $\partial_1 w_0(x_1, x_2)$  for all  $x_1 \in \mathbb{T} \setminus \{x_1^{\vee}(x_2)\}$ , and we have the bounds

$$\partial_1 w_0(x_1^{\vee}(x_2), x_2) \leq -\frac{1}{2\varepsilon}, \qquad \partial_1^3 w_0(x_1^{\vee}(x_2), x_2) \geq \frac{1}{2\varepsilon^3}, \qquad \forall x_2 \in \mathbb{T}.$$

(4) The derivatives in the  $x_1$ -direction cost a factor of  $\varepsilon$ , while the derivatives in the  $x_2$ -direction cost a unit factor. Precisely, for all  $j, k \in \{0, 1, \dots, 4\}$  with  $j + k \le 4$ , we assume that

$$\varepsilon\|\partial_1^j\partial_2^k(w_0-\kappa_0)\|_\infty+\|\partial_1^j\partial_2^kz_0\|_\infty+\|\partial_1^j\partial_2^ka_0\|_\infty+\|\partial_1^j\partial_2^ks_0\|_\infty\leq \tfrac{1}{2}\kappa_0(j+k)!\varepsilon^{-j+1}.$$

With more refined constraints on the initial conditions such as those detailed in Section 4.2 of [8], the Maximal Globally Hyperbolic Development or MGHD was established in [8].

#### 3. EULER IN ALE COORDINATES ADAPTED TO FAST ACOUSTIC CHARACTERISTIC SURFACES

Our CSF algorithm will be founded upon the Arbitrary Lagrangian Eulerian (ALE) coordinate system that was introduced in [8]. We shall define a time-dependent family of ALE transformations that freeze the fast acoustic characteristic surfaces. This family of diffeomorphisms will be constructed using a specific tangential reparameterization of the "Lagrangian" flow of the fast acoustic transport velocity  $v_3$  defined in (2.9)

3.1. A Lagrangian parameterization of the fast characteristic surfaces. With  $t = t_{in}$  denoting the initial time, we let  $\eta(x,t)$  denote the Lagrangian flow of the fact acoustic characteristic velocity  $\mathbf{v}_3 = \mathbf{u} + \alpha \sigma \mathbf{n}$ , satisfying

$$\partial_t \boldsymbol{\eta}(\boldsymbol{x},t) = \boldsymbol{v}_3(\boldsymbol{\eta}(\boldsymbol{x},t),t), \quad t > \mathsf{t}_{\mathsf{in}},$$
 (3.1a)

$$\eta(x, \mathsf{t}_{\mathsf{in}}) = x. \tag{3.1b}$$

The vector n, appearing in the definition of  $v_3$ , denotes the unit normal vector to the fast characteristic surface and is defined by

$$n(\eta(x,t),t) = |\eta_{,2}(x,t)|^{-1} (\eta^{2}_{,2}(x,t), -\eta^{1}_{,2}(x,t)).$$

The unit tangent vector to the fast characteristic surface and is defined by

$$\boldsymbol{\tau}(\boldsymbol{\eta}(\boldsymbol{x},t),t) = |\boldsymbol{\eta}_{,2}\left(\boldsymbol{x},t\right)|^{-1} \left(\eta^{1}_{,2}\left(\boldsymbol{x},t\right),\eta^{2}_{,2}\left(\boldsymbol{x},t\right)\right).$$

At the initial time-slice  $\{t=\mathsf{t}_{\mathsf{in}}\}$ , we foliate  $\mathbb{T}^2$  with lines, parallel to the  $x_2$ -axis, and parameterized by the  $x_1$ -coordinate. From each such  $x_1$ -slice, we emanate the fast acoustic characteristic surface  $\Gamma_{x_1}(T)$ , defined by

$$\Gamma_{x_1}(T) = \left\{ \left( \eta^1(x_1, x_2, t), \eta^2(x_1, x_2, t), t \right) : x_2 \in \mathbb{T}, \ t \in [\mathsf{t}_\mathsf{in}, T] \right\}, \ \ T > \mathsf{t}_\mathsf{in} \ .$$

The intersection of  $\Gamma_{x_1}(T)$  with the time-slice at time t produces the curve  $\gamma_{x_1}(t)$ , defined by

$$\gamma_{x_1}(t) := \{ \eta(x_1, x_2, t) : x_2 \in \mathbb{T} \}, \quad \text{for} \quad x_1 \in \mathbb{T}, t \in [\mathsf{t}_{\mathsf{in}}, T],$$

which we refer to as the *fast acoustic wavefronts*. By definition, the unit normal vector n(y, t) gives the local direction of wavefront propagation, where  $y = \eta(x, t)$  denotes the Eulerian spatial coordinate.

3.2. An ALE parameterization of the fast characteristic surfaces. We now replace the time-dependent family of transformation  $\eta(\cdot,t)$  with a tangentially reparameterized family of maps  $\psi(\cdot,t)$  with flow velocity

$$\partial_t \psi = (\mathbf{v}_3 \cdot \mathbf{n} \, \mathbf{n}) \circ \psi + (\psi_{,2} \cdot \mathbf{e}_1) (\mathbf{v}_3 \cdot \mathbf{n} \, \tau) \circ \psi \,. \tag{3.2}$$

In particular, we introduce the *height function*  $h(x_1, x_2, t)$  and define

$$\psi(x,t) = (h(x_1, x_2, t), x_2, t), \tag{3.3}$$

so that each fast acoustic wave front can be written as

$$\gamma_{x_1}(t) := \{ h(x_1, x_2, t), x_2, t) : x_2 \in \mathbb{T} \}, \quad \text{for} \quad x_1 \in \mathbb{T}, t \in [\mathsf{t}_{\mathsf{in}}, T].$$
 (3.4)

From (3.2), we have that

$$\partial_t h = g^{\frac{1}{2}} (\boldsymbol{v}_3 \cdot \boldsymbol{n}) \circ \boldsymbol{\psi},$$

where the induced metric is defined by

$$g = 1 + (h_{,2})^2$$

and the unit tangent vectors  $\tau$  and normal vectors n to the curves  $\gamma_{x_1}(t)$  are then given by

$$\tau \circ \psi = g^{-\frac{1}{2}}(h, 2, 1), \quad \text{and} \quad n \circ \psi = g^{-\frac{1}{2}}(1, -h, 2).$$
 (3.5)

It is of fundamental importance to accurately track the shape of the fast acoustic characteristic surfaces, and to have an accurate method for evolving the basic geometric vector fields n and  $\tau$ . One of the major advantages of our ALE reparameterization of the Lagrangian flow, is that we are able to avoid grid distortion in the presence of even moderate tangential fluid velocities.

Perhaps the most fundamental geometric quantity is the Jacobian determinant of the  $\nabla \psi(x,t)$ . Shock formation occurs whenever the determinant of the  $\nabla \psi(x,t)$  vanishes. We set

$$J(\boldsymbol{x},t) = \det \boldsymbol{\nabla} \boldsymbol{\psi} = h_{,1} (\boldsymbol{x},t),$$

and define the metric-scaled Jacobian determinant by

$$J_{q}(\mathbf{x},t) = g(x,t)^{-\frac{1}{2}}J(\mathbf{x},t).$$
(3.6)

For an Eulerian variable f(y,t), let  $F(x,t)=f(\psi(x,t),t)$  denote its ALE counterpart. Then,

$$\partial_n f \circ \psi = J_g^{-1} F_{,1} - g^{-\frac{1}{2}} h_{,2} F_{,2} ,$$
 (3.7a)

$$\partial_{\tau} f \circ \psi = g^{-\frac{1}{2}} F_{,2} . \tag{3.7b}$$

Since shock formation occurs at a point (x,t) where  $J_g(x,t) = 0$ , the identity shows that the Eulerian normal derivative  $\partial_n f(\psi(x,t),t)$  becomes infinite whenever the metric-scaled Jacobian determinant  $J_g(x,t)$  vanishes.

We define

$$\Lambda_3 = (\boldsymbol{v}_3 \cdot \boldsymbol{n}) \circ \boldsymbol{\psi}$$
.

The Eulerian transport operator associated with the fast characteristic velocity transforms into a time-derivative with a tangential correction in ALE coordinates:

$$(\partial_t + \boldsymbol{v}_3 \cdot \nabla) f \circ \psi = (\partial_t + V \partial_2) F, \tag{3.8}$$

where

$$V = g^{-\frac{1}{2}}(A - \Lambda_3 h_{,2}). \tag{3.9}$$

3.3. The system of differentiated Riemann variables in ALE coordinates. We shall now write the system of equations (2.31)–(2.30) using our ALE variables adapted to the fast acoustic characteristic surfaces.

In general, we shall employ lowercase letters for Eulerian functions and uppercase letters for ALE functions. We define

$$\mathring{\mathbf{W}}_{n} = \mathring{\mathbf{w}}_{n} \circ \psi, \qquad \mathring{\mathbf{W}}_{\tau} = \mathring{\mathbf{w}}_{\tau} \circ \psi, \qquad \Sigma = \sigma \circ \psi, \qquad U = u \circ \psi. \tag{3.10}$$

We use the lowercase symbols h for the ALE height function and g for the ALE induced metric. The variables  $\mathring{W}_n$  and  $\mathring{W}_{\tau}$  denote the ALE version of the Differentiated Riemann Variables (DRV). For notational simplicity, we continue to denote the ALE version of the matrices in (2.12) and (2.20) by  $\mathbf{C}$ ,  $\mathbf{E}^{\tau}$ , and  $\mathbf{E}^{n}$ , where each component has been composed with  $\psi$ .<sup>4</sup>

In this section we compute the evolution of the classical and differentiated Riemann variables (2.18) and (2.15) in the ALE coordinates  $y = \psi(x, t)$ . Composing the vector Euler equations (2.23) with  $\psi$ , we have that

$$(\partial_t + V \partial_2) \mathbf{W} = \mathbf{G}, \tag{3.11a}$$

$$(\partial_t + V \partial_2) \mathring{\mathbf{W}}_n + J_g^{-1} \mathbf{E}^1 \mathring{\mathbf{W}}_{n,1} + \mathbf{E}^2 \mathring{\mathbf{W}}_{n,2} = \mathring{\mathbf{G}}_n,$$
(3.11b)

$$(\partial_t + V \partial_2) \mathring{\mathbf{W}}_{\tau} + J_a^{-1} \mathbf{E}^1 \mathring{\mathbf{W}}_{\tau, 1} + \mathbf{E}^2 \mathring{\mathbf{W}}_{\tau, 2} = \mathring{\mathbf{G}}_{\tau}, \tag{3.11c}$$

where  $\mathbf{E}^1 = \mathbf{E}^n - \Lambda_3 \mathbf{I}$  and

$$\mathbf{E}^1 = \mathbf{E}^n - \Lambda_3 \mathbf{I} \,, \tag{3.12a}$$

$$\mathbf{E}^{2} = g^{-\frac{1}{2}} (\mathbf{E}^{\tau} - A\mathbf{I} - (\mathbf{E}^{n} - \Lambda_{3}\mathbf{I})h_{,2}) = g^{-\frac{1}{2}} \begin{pmatrix} 2\alpha\Sigma h_{,2} & -\alpha\Sigma & 0 & 0\\ \frac{1}{2}\alpha\Sigma & \alpha\Sigma h_{,2} & -\frac{1}{2}\alpha\Sigma & 0\\ 0 & \alpha\Sigma & 0 & 0\\ 0 & 0 & 0 & \alpha\Sigma h_{,2} \end{pmatrix}.$$
(3.12b)

<sup>&</sup>lt;sup>4</sup>The matrices C,  $E^{\tau}$ , and  $E^n$  are interpreted as ALE variables if they are multiplying the upper-case ALE DRV variables  $\mathring{W}_n$  or  $\mathring{W}_{\tau}$ .

and where

$$\mathring{\boldsymbol{G}}_{n} = \mathring{\boldsymbol{g}}_{n} \circ \boldsymbol{\psi} , \quad \mathring{\boldsymbol{G}}_{\tau} = \mathring{\boldsymbol{g}}_{\tau} \circ \boldsymbol{\psi} , \quad \boldsymbol{G} = -\mathbf{E}^{1} \mathring{\boldsymbol{W}}_{n} - (\mathbf{E}^{\tau} - A\mathbf{I}) \mathring{\boldsymbol{W}}_{\tau} + \begin{pmatrix} -A(\frac{1+\alpha}{2}W_{\tau} + \frac{1-\alpha}{2}Z_{\tau} + \frac{\alpha\Sigma}{4\alpha+2}S_{\tau}) \\ -A(\frac{1+\alpha}{2}\mathring{W}_{\tau} + \frac{1-\alpha}{2}\mathring{Z}_{\tau} + \frac{\alpha\Sigma}{4\alpha+2}\mathring{S}_{\tau}) \\ \frac{1}{2}(W+Z)(\frac{1+\alpha}{2}\mathring{W}_{\tau} + \frac{1-\alpha}{2}\mathring{Z}_{\tau} + \frac{\alpha\Sigma}{4\alpha+2}\mathring{S}_{\tau}) \\ 0 \end{pmatrix} \circ \boldsymbol{\psi}$$

Multiplying (3.11b) by  $J_g$  and commuting around the partial derivatives yields

$$(\partial_t + V\partial_2)(J_a \mathring{\boldsymbol{W}}_n) + \mathbf{E}^1 \mathring{\boldsymbol{W}}_{n,1} + \mathbf{E}^2 (J_a \mathring{\boldsymbol{W}}_n)_{,2} = J_a \mathring{\boldsymbol{G}}_n - \mathring{\boldsymbol{W}}_n (\partial_t + V\partial_2) J_a - J_{a,2} \mathbf{E}^2 \mathring{\boldsymbol{W}}_n. \tag{3.13}$$

Writing the geometric terms (2.25) in ALE coordinates,

$$K_t = \frac{1+\alpha}{2}\mathring{W}_{\tau} + \frac{1-\alpha}{2}\mathring{Z}_{\tau} + \frac{\alpha\Sigma}{4\alpha+2}\mathring{S}_{\tau}, \qquad K_n = g^{-\frac{1}{2}}J_g^{-1}J_{g,2}, \qquad K_{\tau} = g^{-\frac{3}{2}}h_{,22}, \qquad (3.14)$$

the componentwise equations (3.13) in terms of the differentiated Riemann variables become

$$(\partial_{t} + V \partial_{2})(J_{g}\mathring{W}_{n}) - \alpha \Sigma(J_{g}\mathring{A}_{n})_{,2} = J_{g}\mathring{Z}_{n}(\frac{\alpha}{2}\Sigma g^{-\frac{3}{2}}h_{,22}) + J_{g}\mathring{A}_{n}(\alpha \Sigma g^{-\frac{1}{2}}J_{g}^{-1}J_{g,2} - \frac{1+\alpha}{2}\mathring{W}_{\tau} - \frac{1-\alpha}{2}\mathring{Z}_{\tau}$$

$$- \frac{\alpha\Sigma}{4\alpha+2}\mathring{S}_{\tau}) + J_{g}\mathring{W}_{n}(\frac{\alpha}{2}\Sigma g^{-\frac{3}{2}}h_{,22}) + J_{g}\mathring{S}_{n}(-\frac{\alpha\Sigma}{4\alpha+2}(\frac{1}{2}\mathring{W}_{n} + \frac{3}{2}\mathring{Z}_{n} + \mathring{A}_{\tau} - \frac{2\Sigma}{4\alpha+2}))$$

$$+ J_{g}\mathring{A}_{\tau}(-\frac{\alpha}{2}(\mathring{W}_{n} - \mathring{Z}_{n}) - \frac{\Sigma}{4\alpha+2}\mathring{S}_{n} - \alpha\Sigma g^{-\frac{3}{2}}h_{,22}) + J_{g}\mathring{W}_{\tau}(-\mathring{A}_{n} - \frac{1+\alpha}{2}\mathring{W}_{\tau} - \frac{1-\alpha}{2}\mathring{Z}_{\tau}$$

$$- \frac{\alpha\Sigma}{4\alpha+2}\mathring{S}_{\tau}),$$

$$(3.15a)$$

$$(\partial_{t} + V \partial_{2})(J_{g} \mathring{Z}_{n}) - 2\alpha \Sigma \mathring{Z}_{n,1} + 2\alpha \Sigma g^{-\frac{1}{2}} h_{,2} (J_{g} \mathring{Z}_{n})_{,2} - \alpha \Sigma \mathring{A}_{n,2} = J_{g} \mathring{Z}_{n} (\alpha(\mathring{W}_{n} - \mathring{Z}_{n}) + \frac{2\alpha \Sigma}{4\alpha + 2} \mathring{S}_{n}$$

$$+ 2\alpha \Sigma g^{-\frac{1}{2}} h_{,2} J_{g}^{-1} J_{g,2} - \frac{1}{2} \alpha \Sigma g^{-\frac{3}{2}} h_{,22}) + J_{g} \mathring{A}_{n} (\alpha \Sigma g^{-\frac{1}{2}} J_{g}^{-1} J_{g,2} - \frac{1+\alpha}{2} \mathring{W}_{\tau} - \frac{1-\alpha}{2} \mathring{Z}_{\tau}$$

$$- \frac{\alpha \Sigma}{4\alpha + 2} \mathring{S}_{\tau}) + J_{g} \mathring{W}_{n} (-\frac{1}{2} \alpha \Sigma g^{-\frac{3}{2}} h_{,22}) + J_{g} \mathring{S}_{n} (-\frac{\alpha \Sigma}{4\alpha + 2} (\frac{1}{2} (\mathring{W}_{n} + \mathring{Z}_{n}) + \mathring{A}_{\tau}))$$

$$+ J_{g} \mathring{Z}_{\tau} (2\alpha \Sigma g^{-\frac{1}{2}} J_{g}^{-1} J_{g,2} - \mathring{A}_{n} - \frac{1+\alpha}{2} \mathring{W}_{\tau} - \frac{1-\alpha}{2} \mathring{Z}_{\tau} - \frac{\alpha \Sigma}{4\alpha + 2} \mathring{S}_{\tau})$$

$$+ J_{g} \mathring{A}_{\tau} (\frac{\alpha}{2} (\mathring{W}_{n} - \mathring{Z}_{n}) + \frac{\alpha \Sigma}{4\alpha + 2} \mathring{S}_{n} + \alpha \Sigma g^{-\frac{3}{2}} h_{,22}),$$

$$(3.15b)$$

$$\begin{split} (\partial_{t} + V \partial_{2})(J_{g} \mathring{A}_{n}) - \alpha \Sigma \mathring{A}_{n,1} + \alpha \Sigma g^{-\frac{1}{2}} h_{,2} (J_{g} \mathring{A}_{n})_{,2} - \frac{\alpha}{2} \Sigma (J_{g} \mathring{W}_{n} - J_{g} \mathring{Z}_{n})_{,2} &= J_{g} \mathring{Z}_{n} (\frac{1+\alpha}{2} \mathring{W}_{\tau} + \frac{1-\alpha}{2} \mathring{Z}_{\tau} \\ &+ \frac{\alpha \Sigma}{4\alpha + 2} \mathring{S}_{\tau} - \alpha \Sigma g^{-\frac{1}{2}} J_{g}^{-1} J_{g,2}) + J_{g} \mathring{A}_{n} (\frac{\alpha}{2} (\mathring{W}_{n} - \mathring{Z}_{n}) + \frac{\alpha \Sigma}{4\alpha + 2} \mathring{S}_{n} + \alpha \Sigma g^{-\frac{1}{2}} h_{,2} J_{g}^{-1} J_{g,2}) \\ &+ J_{g} \mathring{W}_{n} (\frac{1+\alpha}{4} \mathring{W}_{\tau} + \frac{1-\alpha}{4} \mathring{Z}_{\tau} + \frac{\alpha \Sigma}{8\alpha + 4} \mathring{S}_{\tau}) + J_{g} \mathring{S}_{n} (-\frac{\alpha \Sigma}{4\alpha + 2} (\frac{1}{2} (\mathring{W}_{\tau} - \mathring{Z}_{\tau}) + \frac{\Sigma}{4\alpha + 2} \mathring{S}_{\tau})) \\ &+ J_{g} \mathring{Z}_{\tau} (\frac{\alpha}{2} (\mathring{W}_{n} - \mathring{Z}_{n}) + \frac{\alpha \Sigma}{4\alpha + 2} \mathring{S}_{n} - \alpha \Sigma g^{-\frac{3}{2}} h_{,22}) + J_{g} \mathring{A}_{\tau} (-\frac{1+\alpha}{2} \mathring{W}_{\tau} - \frac{1-\alpha}{2} \mathring{Z}_{\tau} - \frac{\alpha \Sigma}{4\alpha + 2} \mathring{S}_{\tau}) \\ &+ \alpha \Sigma g^{-\frac{1}{2}} J_{g}^{-1} J_{g,2} - \mathring{A}_{n}) + J_{g} \mathring{W}_{\tau} (-\frac{\alpha}{4} (\mathring{W}_{n} - \mathring{Z}_{n}) - \frac{\alpha \Sigma}{8\alpha + 4} \mathring{S}_{\tau} + \alpha \Sigma g^{-\frac{3}{2}} h_{,22}) \\ &+ J_{g} \mathring{S}_{\tau} (\frac{\alpha \Sigma}{4\alpha + 2} (\frac{1}{2} (\mathring{W}_{n} - \mathring{Z}_{n}) + \frac{\Sigma}{4\alpha + 2} \mathring{S}_{n})), \end{split}$$

$$(\partial_t + V \partial_2)(J_g \mathring{S}_n) - \alpha \Sigma \mathring{S}_n,_1 + \alpha \Sigma g^{-\frac{1}{2}} h,_2 (J_g \mathring{S}_n),_2 = J_g \mathring{S}_n (\frac{\alpha}{2} (\mathring{W}_n + \mathring{Z}_n) + \frac{\alpha \Sigma}{4\alpha + 2} \mathring{S}_n + \alpha \Sigma g^{-\frac{1}{2}} J_g^{-1} J_{g,2})$$

$$+ J_g \mathring{S}_\tau (-\frac{1+\alpha}{2} \mathring{W}_\tau - \frac{1-\alpha}{2} \mathring{Z}_\tau - \frac{\alpha \Sigma}{4\alpha + 2} \mathring{S}_\tau - \mathring{A}_n + \alpha \Sigma g^{-\frac{3}{2}} h,_{22}).$$
(3.15d)

Similarly, (3.11c) becomes

$$(\partial_{t} + V\partial_{2})\mathring{W}_{\tau} - \alpha\Sigma\mathring{A}_{\tau,2} = \mathring{A}_{n}(\alpha\Sigma g^{-\frac{3}{2}}h_{,22}) + \mathring{S}_{n}(\frac{\alpha\Sigma}{4\alpha+2}(\frac{1}{2}(\mathring{W}_{\tau} - \mathring{Z}_{\tau}) + \frac{\Sigma}{4\alpha+2}\mathring{S}_{\tau})) + \mathring{Z}_{\tau}(\frac{\alpha}{2}\Sigma g^{-\frac{3}{2}}h_{,22})$$

$$+ \mathring{A}_{\tau}(-\frac{1+2\alpha}{2}\mathring{W}_{\tau} - \frac{1-2\alpha}{2}\mathring{Z}_{\tau} - \frac{2\alpha\Sigma}{4\alpha+2}\mathring{S}_{\tau}) + \mathring{W}_{\tau}(\frac{\alpha}{2}\Sigma g^{-\frac{3}{2}}h_{,22} - \mathring{A}_{\tau})$$

$$+ \mathring{S}_{\tau}(-\frac{\alpha\Sigma}{4\alpha+2}(\mathring{Z}_{n} + \mathring{A}_{\tau} - \frac{\Sigma}{4\alpha+2}\mathring{S}_{n})),$$

$$(3.16a)$$

$$(\partial_{t} + V\partial_{2})\mathring{Z}_{\tau} - 2\alpha\Sigma J_{g}^{-1}\mathring{Z}_{\tau,1} + 2\alpha\Sigma g^{-\frac{1}{2}}h_{,2}\mathring{Z}_{\tau,2} + \alpha\Sigma\mathring{A}_{\tau,2} = \mathring{Z}_{n}(\alpha(\mathring{W}_{\tau} - \mathring{Z}_{\tau}) + \frac{2\alpha\Sigma}{4\alpha+2}\mathring{S}_{\tau}$$

$$- 2\alpha\Sigma g^{-\frac{1}{2}}J_{g}^{-1}J_{g,2}) + \mathring{A}_{n}(-\alpha\Sigma g^{-\frac{3}{2}}h_{,22}) + \mathring{S}_{n}(\frac{\alpha\Sigma}{4\alpha+2}(\frac{1}{2}(\mathring{W}_{\tau} - \mathring{Z}_{\tau}) + \frac{\Sigma}{4\alpha+2}\mathring{S}_{\tau})$$

$$+ \mathring{Z}_{\tau}(-\mathring{A}_{\tau} - \frac{\alpha}{2}\Sigma g^{-\frac{3}{2}}h_{,22}) + \mathring{A}_{\tau}(2\alpha\Sigma g^{-\frac{1}{2}}J_{g}^{-1}J_{g,2} - \frac{1}{2}(\mathring{W}_{\tau} + \mathring{Z}_{\tau})) + \mathring{W}_{\tau}(-\frac{\alpha}{2}\Sigma g^{-\frac{3}{2}}h_{,22})$$

$$+ \mathring{S}_{\tau}(-\frac{\alpha\Sigma}{4\alpha+2}(\mathring{W}_{n} + \mathring{A}_{\tau} + \frac{\Sigma}{4\alpha+2}\mathring{S}_{n})),$$

$$(3.16b)$$

$$(\partial_{t} + V\partial_{2})\mathring{A}_{\tau} - \alpha\Sigma J_{g}^{-1}\mathring{A}_{\tau,1} + \alpha\Sigma g^{-\frac{1}{2}}h_{,2}\mathring{A}_{\tau,2} + \frac{\alpha}{2}\Sigma(\mathring{W}_{\tau} - \mathring{Z}_{\tau})_{,2} = \mathring{Z}_{n}(\alpha(\mathring{W}_{n} - \mathring{Z}_{n}) + \frac{2\alpha\Sigma}{4\alpha+2}\mathring{S}_{n}$$

$$- 2\alpha\Sigma g^{-\frac{1}{2}}J_{g}^{-1}J_{g,2}) + \mathring{A}_{n}(-\alpha\Sigma g^{-\frac{3}{2}}h_{,22}) + \mathring{W}_{n}(-\alpha\Sigma g^{-\frac{3}{2}}h_{,22}) + \mathring{Z}_{\tau}(\frac{1+2\alpha}{4}\mathring{W}_{\tau} + \frac{1-2\alpha}{4}\mathring{Z}_{\tau}$$

$$+\frac{\alpha\Sigma}{4\alpha+2}\mathring{S}_{\tau} - \alpha\Sigma g^{-\frac{1}{2}}J_{g}^{-1}J_{g,2}) - \mathring{A}_{\tau}^{2} + \mathring{W}_{\tau}(\frac{1}{4}(\mathring{W}_{\tau} - \mathring{Z}_{\tau}) - \frac{\alpha}{2}\Sigma g^{-\frac{1}{2}}J_{g}^{-1}J_{g,2}),$$
(3.16c)

$$(\partial_t + V \partial_2) \mathring{S}_{\tau} - \alpha \Sigma \mathring{S}_{n,1} + \alpha \Sigma g^{-\frac{1}{2}} h_{,2} \mathring{S}_{\tau,2} = \mathring{S}_n (\frac{\alpha}{2} (\mathring{W}_n - \mathring{Z}_n) + \frac{\alpha \Sigma}{4\alpha + 2} \mathring{S}_n - \alpha \Sigma g^{-\frac{1}{2}} J_g^{-1} J_{g,2}) - \mathring{S}_{\tau} \mathring{A}_{\tau}.$$
(3.16d)

Equation (3.11a) becomes

$$(\partial_t + V \partial_2)W + \alpha \Sigma \mathring{A}_\tau = -A(\frac{1+\alpha}{2}\mathring{W}_\tau + \frac{1-\alpha}{2}\mathring{Z}_\tau + \frac{\alpha\Sigma}{4\alpha+2}\mathring{S}_\tau) + \frac{\alpha\Sigma^2}{4\alpha+2}\mathring{S}_n,$$
(3.17a)

$$(\partial_t + V \partial_2) Z - 2\alpha \Sigma \mathring{Z}_n - \alpha \Sigma \mathring{A}_\tau = -A(\frac{1+\alpha}{2}\mathring{W}_\tau + \frac{1-\alpha}{2}\mathring{Z}_\tau + \frac{\alpha \Sigma}{4\alpha+2}\mathring{S}_\tau) - \frac{\alpha \Sigma^2}{4\alpha+2}\mathring{S}_n,$$
(3.17b)

$$(\partial_t + V\partial_2)A - \alpha \Sigma \mathring{A}_n - \frac{\alpha}{2} \Sigma (\mathring{W}_\tau - \mathring{Z}_\tau) = \frac{1}{2} (W + Z) \left( \frac{1+\alpha}{2} \mathring{W}_\tau + \frac{1-\alpha}{2} \mathring{Z}_\tau + \frac{\alpha \Sigma}{4\alpha + 2} \mathring{S}_\tau \right), \tag{3.17c}$$

$$(\partial_t + V \partial_2) S - \alpha \Sigma \mathring{S}_n = 0. \tag{3.17d}$$

Finally, the evolution equations for  $h_2$  and  $J_q$  are

$$(\partial_t + V \partial_2)h_{,2} = g(\frac{1+\alpha}{2}\mathring{W}_\tau + \frac{1-\alpha}{2}\mathring{Z}_\tau + \frac{\alpha\Sigma}{4\alpha+2}\mathring{S}_\tau), \tag{3.18a}$$

$$(\partial_t + V \partial_2) J_g = J_g \left( \frac{1+\alpha}{2} \mathring{W}_n + \frac{1-\alpha}{2} \mathring{Z}_n + \frac{\alpha \Sigma}{4\alpha + 2} \mathring{S}_n \right), \tag{3.18b}$$

and we have that

$$\partial_t h = g^{\frac{1}{2}} \left( \frac{1+\alpha}{2} W + \frac{1-\alpha}{2} Z \right). \tag{3.19}$$

Equations (3.15)–(3.18) form a complete set of evolution equations for the variables

$$\mathbf{\Pi}(\boldsymbol{x},t) := (W, Z, A, S, J_g \mathring{W}_n, J_g \mathring{Z}_n, J_g \mathring{A}_n, J_g \mathring{S}_n, \mathring{W}_{\tau}, \mathring{Z}_{\tau}, \mathring{A}_{\tau}, \mathring{S}_{\tau}, J_g, h, 2, h). \tag{3.20}$$

We will divide our dependent variables  $\Pi$  into an undifferentiated part  $\Pi=(W,Z,A,S,h)$ , and a differentiated part  $\mathring{\Pi}=(J_g\mathring{W}_n,J_g\mathring{Z}_n,J_g\mathring{A}_n,J_g\mathring{S}_n,\mathring{W}_{\tau},\mathring{Z}_{\tau},\mathring{A}_{\tau},\mathring{S}_{\tau},J_g,h,_2)$ . Given functions  $(w_0,z_0,a_0,s_0)\in H^7(\mathbb{T}^2)$ , full initial conditions for the DRV system (3.15)–(3.18) are given by

$$W(\boldsymbol{x},0) = w_0(\boldsymbol{x}), \qquad (J_{\sigma} \mathring{\boldsymbol{W}}_n)(\boldsymbol{x},0) = \partial_1 w_0(\boldsymbol{x}), \qquad \mathring{\boldsymbol{W}}_{\tau}(\boldsymbol{x},0) = \partial_2 w_0(\boldsymbol{x}), \qquad (3.21a)$$

$$Z(\boldsymbol{x},0) = z_0(\boldsymbol{x}), \qquad (J_g \mathring{\boldsymbol{Z}}_n)(\boldsymbol{x},0) = \partial_1 z_0(\boldsymbol{x}), \qquad \mathring{\boldsymbol{Z}}_\tau(\boldsymbol{x},0) = \partial_2 z_0(\boldsymbol{x}), \qquad (3.21b)$$

$$A(\boldsymbol{x},0) = a_0(\boldsymbol{x}), \qquad (J_g \mathring{\boldsymbol{A}}_n)(\boldsymbol{x},0) = \partial_1 a_0(\boldsymbol{x}), \qquad \mathring{\boldsymbol{A}}_\tau(\boldsymbol{x},0) = \partial_2 a_0(\boldsymbol{x}), \qquad (3.21c)$$

$$S(\boldsymbol{x},0) = s_0(\boldsymbol{x}), \qquad (J_a \mathring{\boldsymbol{S}}_n)(\boldsymbol{x},0) = \partial_1 s_0(\boldsymbol{x}), \qquad \mathring{\boldsymbol{S}}_{\tau}(\boldsymbol{x},0) = \partial_2 s_0(\boldsymbol{x}), \qquad (3.21d)$$

$$h(\mathbf{x},0) = x_1,$$
  $J_a(\mathbf{x},0) = 1,$   $h_{,2}(x,0) = 0.$  (3.21e)

We shall refer to equations (3.15)–(3.18) with initial conditions of the form (3.21) as the *DRV system*. Note that we include h into our set of unknowns as it will be convenient to numerically track the fast acoustic wavefronts.

3.4. Fractional-order expansions of the Euler solution at  $t = T^*$ . As we have noted above, using initial data satisfying the conditions of Section 4.2 in [8], the MGHD was established in Theorems 4.6, 4.7, and 4.8 in [8]. With  $(y^*, T^*)$  denoting the location of the first gradient singularity in Eulerian spacetime (or equivalently, the minimum of the pre-shock set), together with the fractional-order expansions for the Euler solution about the pre-shock presented in [1] and [6], we have the following Puiseux expansions about  $y = y^*$  at the time  $t = T^*$ :

$$w(y_1, y_2^*, T^*) = c_0^w + c_1^w (y_1 - y_1^*)^{\frac{1}{3}} + O(|y_1 - y_1^*|^{\frac{2}{3}}),$$
(3.22a)

$$z(y_1, y_2^*, T^*) = c_0^z + c_3^z(y_1 - y_1^*) + c_4^z(y_1 - y_1^*)^{\frac{4}{3}} + O(|y_1 - y_1^*|^{\frac{5}{3}}),$$
(3.22b)

$$a(y_1, y_2^*, T^*) = c_0^a + c_3^a(y_1 - y_1^*) + c_4^a(y_1 - y_1^*)^{\frac{4}{3}} + O(|y_1 - y_1^*|^{\frac{5}{3}}),$$
(3.22c)

$$s(y_1, y_2^*, T^*) = c_0^s + c_3^s(y_1 - y_1^*) + c_4^s(y_1 - y_1^*)^{\frac{4}{3}} + O(|y_1 - y_1^*|^{\frac{5}{3}}),$$
(3.22d)

for constants  $c_i^w, c_i^z, c_i^a, c_i^s \in \mathbb{R}, j=0,1, i=0,3,4.$  We also have that

$$u_1(y_1, y_2^*, T^*) = c_0^{u_1} + c_1^{u_1} (y_1 - y_1^*)^{\frac{1}{3}} + O(|y_1 - y_1^*|^{\frac{2}{3}}),$$
(3.23a)

$$u_2(y_1, y_2^*, T^*) = c_0^{u_2} + c_1^{u_2} (y_1 - y_1^*)^{\frac{1}{3}} + O(|y_1 - y_1^*|^{\frac{2}{3}}),$$
(3.23b)

$$\sigma(y_1, y_2^*, T^*) = c_0^{\sigma} + c_1^{\sigma}(y_1 - y_1^*)^{\frac{1}{3}} + O(|y_1 - y_1^*|^{\frac{2}{3}}), \tag{3.23c}$$

for constants  $c_i^{u_1}, c_i^{u_2}, c_i^{\sigma} \in \mathbb{R}$ , i=0,1. Formulas for the coefficients  $c_i^q$  in terms of the ALE variables  $\Pi$  and their derivatives are given in Appendix A.

## 3.5. Solving the Euler equations on the spacetime set $\Omega^*$ .

3.5.1. Geometric description for the curve of pre-shocks. In (1.2), we defined the spacetime set that is bounded from above by the curve of pre-shocks, parameterized by the curve  $x_1 = X_1^*(x_2)$  and  $t = t^*(x_2)$ . We shall now provide a geometric description of the pre-shock in terms of the rescaled Jacobian determinant  $J_g$ . As we have noted above, shock formation occurs for labels  $x^*$  and times  $t^*$  for which  $J_g(x^*, t^*) = 0$ . As shown in Figure 3, the so-called singular shown in red, is the level set  $\{J_g = 0\}$ . This singular hypersurface contains a continuum of Eulerian gradient catastrophes which successively occur as the propagating sound wave progressively steepens. This singular set is, roughly speaking, one-half of an upward facing paraboloid emanating for the curve of pre-shocks which is shown as the black curve in Figure 3. The curve of pre-shocks can be viewed as the set of "first gradient singularity" in that for each transverse coordinate  $x_2 \in \mathbb{T}$ , there exists a first blowup time  $t^*(x_2)$ , and an  $x_1$ -component of a blowup label, denoted by  $X_1^*(x_2)$ , such that  $J_g(X_1^*(x_2), x_2, t^*(x_2)) = 0$ . Since the singular set where  $\{J_g = 0\}$  is an upward paraboloid, for  $x_1 > X_1^*(x_2)$ , it follows that  $J_g(x_1, x_2, t^*(x_2)) > 0$  and hence that  $\partial_1 J_{g_1}, x_2, t^*(x_2) > 0$ .

In fact, the conditions that  $J_g, 1 > 0$  and  $J_g, 1 < 0$  split the spacetime into what we call the *downstream* and *upstream* regions, respectively. The interface between these two regions is the level-set  $\{J_g, 1=0\}$ , which is displayed as the nearly vertical magenta surface in Figure 3. Geometrically, the curve of pre-shocks (shown as the black curve in Figure 3) is the intersection of the singular set  $\{J_g=0\}$  (shown in red) and the interface between the upstream and downstream regions of spacetime  $\{J_g, 1=0\}$  (shown in magenta).

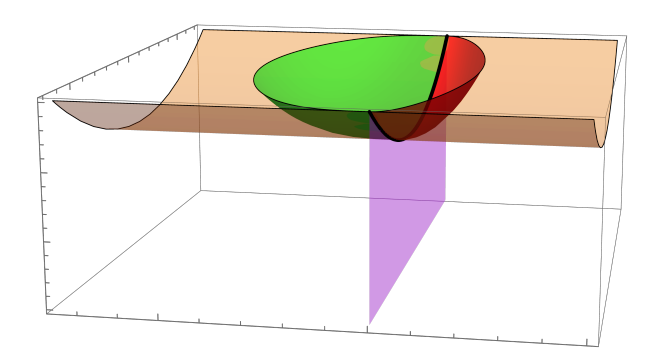


FIGURE 3. Four fundamental hypersurfaces are displayed. The "nearly vertical" surface  $x_1=x_1^*(x_2,t):=\mathop{\rm argmin}_{x_1\in\mathbb{T}}J_g(x_1,x_2,t)$  is shown in magenta. This surface passes through the set of pre-shocks, displayed as the black curve. In red, the downstream surface  $\{J_g(x,t)=0\}$  is displayed, and in green, the upstream slow acoustic characteristic surface that passes through the pre-shock set is shown. In orange, the cylindrical surface  $t=t^*(x_2)$  is displayed, where  $t^*(x_2)$  denotes the time coordinate along the set of pre-shocks.

We can now give a precise definition for the pre-shock set, which we shall denote by  $\Xi^*$ , as well as its parameterization. Following [8], we define

$$\Xi^* := \{ (\boldsymbol{x}, t) \in \mathbb{T}^2 \times [\mathsf{t}_{\mathsf{in}}, \mathsf{t}_{\mathsf{fin}}] \colon J_q(\boldsymbol{x}, t) = 0 \text{ and } J_{q,1}(\boldsymbol{x}, t) = 0 \} = \{ J_q = 0 \} \cap \{ J_{q,1} = 0 \}. \tag{3.24}$$

We then define a parameterization for  $\{J_{g,1}=0\}$  by  $x_1=x_1^*(x_2,t)$ , where for  $t>t_{\rm in}$ ,

$$x_{1}^{*}(x_{2}, t) = \underset{x_{1} \in \mathbb{T}}{\operatorname{argmin}} J_{g}(x_{1}, x_{2}, t) = \{\{(\boldsymbol{x}, t) \in \mathbb{T}^{2} \times (\mathsf{t}_{\mathsf{in}}, \mathsf{t}_{\mathsf{fin}}] : J_{g, 1}(\boldsymbol{x}, t) = 0\}. \tag{3.25}$$

We will define  $x_1^*(x_2, t = t_{in})$  below via a limit. We can then define the set of times  $t = t^*(x_2)$  along the pre-shock curve as the solutions to

$$J_{q}(x_{1}^{*}(x_{2}, t^{*}(x_{2})), x_{2}, t_{*}(x_{2})) = 0 \text{ for each } x_{2} \in \mathbb{T}.$$
(3.26)

It follows that  $X_1^*(x_2) = x_1^*(x_2, t^*(x_2)).$ 

3.5.2. Flatting the future temporal boundary of  $\Omega^*$ . We now define a new time coordinate s by

$$s = q(x_2, t) = 1 - J_a(x_1^*(x_2, t), x_2, t).$$
(3.27)

From (3.26), we see that

$$q({t = t^*(x_2)}) = {s = 1}.$$

Moreover, since  $J_q(x, t_{in}) = 1$ , it follows that

$$q(\{t = t_{in}\}) = \{s = 0\}. \tag{3.28}$$

The spacetime is transformed as

$$q(\Omega^*) = \mathbb{T}^2 \times [0,1].$$

The temporal remapping function q allows us to devise a computational shock formation algorithm evolve the smooth Euler solution up to the pre-shock curve of first gradient blowups, while using standard horizontal time-slices for the evolution. The fact that the initial time-slice is mapped to another horizontal time-slice allows for the use of the same initial conditions in both systems of coordinates.

Since (3.25) yields  $J_{q,1}(x_1^*(x_2,t),x_2,t)=0$  in  $\Omega^*$ , by differentiating (3.27) and we obtain that

$$\partial_t s = -\partial_t J_g(x_1^*(x_2, t), x_2, t), \qquad \partial_2 s = -J_{g,2}(x_1^*(x_2, t), x_2, t), \qquad (3.29)$$

Letting

$$t = \theta(x_2, s)$$
 where  $\theta = q^{-1}$ 

denotes the inverse map, we have by the inverse function theorem and (3.29) that

$$\partial_s \theta(x_2, s) = -\frac{1}{\partial_t J_g(\xi(x_2, s), x_2, \theta(x_2, s))}, \qquad \theta_{,2}(x_2, s) = -\frac{J_{g,2}(\xi(x_2, s), x_2, \theta(x_2, s))}{\partial_t J_g(\xi(x_2, s), x_2, \theta(x_2, s))}. \tag{3.30}$$

Let us now define the function

$$\xi(x_2, s) = x_1^*(x_2, \theta(x_2, s)) \text{ for } s \in (0, 1].$$
(3.31)

Since  $J_g(x, s = 0) \equiv 1$ , we define  $\xi(x_2, s = 0)$  by the following limit: By continuity that

$$\xi(x_2,0) = \lim_{t \to 0^+} \left( \underset{x_1 \in \mathbb{T}}{\operatorname{argmin}} J_g(\boldsymbol{x},t) \right).$$

Using Taylor's theorem, the evolution equation (3.18b) for  $J_g$ , and the initial conditions (3.21) for  $J_g$  and  $J_g \mathring{W}_n$ , we have that

$$J_g(\boldsymbol{x},t) = 1 + t \big( \tfrac{1+\alpha}{2} \partial_1 w_0(\boldsymbol{x}) + \tfrac{1-\alpha}{2} \partial_1 z_0(\boldsymbol{x}) + \tfrac{\alpha \sigma_0(\boldsymbol{x})}{4\alpha+2} \partial_1 s_0(\boldsymbol{x}) \big) + O(t^2) \text{ as } t \to 0^+ \ .$$

It follows that

$$\xi(x_2, 0) = \operatorname*{argmin}_{x_1 \in \mathbb{T}} \left( \frac{1+\alpha}{2} \partial_1 w_0 + \frac{1-\alpha}{2} \partial_1 z_0 + \frac{\alpha \sigma_0}{4\alpha + 2} \partial_1 s_0 \right). \tag{3.32}$$

Next, by (3.25), we have that

$$J_{g,1}(\xi(x_2,s),x_2,\theta(x_2,s))=0$$
.

Differentiating this identity, and using the chain rule together with (3.30), we find that

$$\partial_s \xi(x_2, s) = -\frac{\partial_t J_{g,1}(\xi(x_2, s), x_2, \theta(x_2, s))}{J_{g,11}(\xi(x_2, s), x_2, \theta(x_2, s)) \partial_t J_g(\xi(x_2, s), x_2, \theta(x_2, s))}$$
(3.33)

The pre-shock curve  $\Xi^*$  defined in (3.24) can then be parameterized as

$$\Xi^* = \{ (\xi(x_2, 1), x_2, \theta(x_2, 1)) : x_2 \in \mathbb{T} \}.$$
(3.34)

We note that by Corollary 6.2 in [8], the use of smooth, compressive, and generic initial conditions satisfying Definition 2.1 ensures that the denominators in (3.30) and (3.33) are not equal to zero.

3.5.3. Dependent variables in the re-mapped spacetime. Given a quantity  $F: \Omega^* \to \mathbb{R}$ , we define the associated quantity in the flattened spacetime by  $\widetilde{F}: \mathbb{T}^2 \times [0,1] \to \mathbb{R}$ ,

$$\widetilde{F}(x, s) = F(x, t)$$
 where  $s = 1 - J_g(x_1^*(x_2, t), x_2, t)$ ,

and the restriction of this function to the surface  $x_1 = \xi(x_2, s)$  is denoted by

$$\overline{F}(x_2, s) = F(\xi(x_2, s), x_2, \theta(x_2, s)).$$

Applying the chain-rule to (3.27), we have that

$$\partial_t F(\boldsymbol{x}, t) = -\partial_t J_g(\xi(x_2, s), x_2, \theta(x_2, s)) \partial_s \tilde{F}(\boldsymbol{x}, s), \qquad (3.35a)$$

$$\partial_1 F(\mathbf{x}, t) = \partial_1 \tilde{F}(\mathbf{x}, s),$$
 (3.35b)

$$\partial_2 F(\boldsymbol{x}, t) = \left(\partial_2 - J_{g,2}\left(\left(\xi(x_2, s), x_2, \theta(x_2, s)\right)\partial_s\right)\tilde{F}(\boldsymbol{x}, s)\right). \tag{3.35c}$$

We also have that

$$(\partial_t + V\partial_2)F(\boldsymbol{x},t) = \left( (Q + (\widetilde{V} - \overline{V})Q_2)\partial_s + \widetilde{V}\partial_2 \right) \tilde{F}(\boldsymbol{x},s)$$
(3.35d)

where

$$Q = -\left(\frac{1+\alpha}{2}\overline{J_g}\mathring{W}_n + \frac{1-\alpha}{2}\overline{J_g}\mathring{Z}_n + \frac{\alpha\overline{\Sigma}}{4\alpha+2}\overline{J_g}\mathring{S}_n\right), \qquad Q_2 = -\overline{J_{g,2}}. \tag{3.36}$$

For notational ease, we shall henceforth drop the *tilde* notation for functions of (x, s). With our new time coordinate s defined, we can transform the Euler evolution in (x, t) coordinates to Euler evolution in (x, s) coordinates. The system of equations (3.11) in (x, s) coordinates takes the following form:

$$\left( \left( Q + (V - \overline{V})Q_2 \right) \partial_s + V \partial_2 \right) \mathbf{W} = \mathbf{G}, \tag{3.37a}$$

$$\mathbf{M}\partial_s(J_g\mathring{\mathbf{W}}_n) + \mathbf{E}^1\partial_1(J_g\mathring{\mathbf{W}}_n) + (\mathbf{E}^2 + V\mathbf{I})\partial_2(J_g\mathring{\mathbf{W}}_n) = J_g\mathring{\mathbf{G}}_n,$$
(3.37b)

$$\mathbf{M}\partial_{s}\mathring{\mathbf{W}}_{\tau} + \mathbf{E}^{1}\partial_{1}\mathring{\mathbf{W}}_{\tau} + (\mathbf{E}^{2} + V\mathbf{I})\partial_{2}\mathring{\mathbf{W}}_{\tau} = \mathring{\mathbf{G}}_{\tau}, \tag{3.37c}$$

where **M** is the  $4 \times 4$  matrix

$$\mathbf{M} = (Q + (V - \overline{V})Q_2)\mathbf{I} + Q_2\mathbf{E}^2$$

and where the matrices  $\mathbf{E}^n$  and  $\mathbf{E}^{\tau}$  are defined in (2.20) and the matrices  $\mathbf{E}^1$  and  $\mathbf{E}^2$  are defined in (3.12), but with the derivative modifications

$$\partial_2 \mapsto \left(\partial_2 - J_{g,2}\left(\left(\xi(x_2, s), x_2, \theta(x_2, s)\right)\partial_s\right) = \left(\partial_2 + Q_2\partial_s\right). \tag{3.38}$$

We note that if the initial data are chosen to satisfy the conditions of Definition 2.1, then the matrix  $\mathbf{M}$  is invertible. The evolution equations (3.18) in  $(\mathbf{x}, s)$  coordinates are written as

$$\left(\left(Q + (V - \overline{V})Q_2\right)\partial_s + V\partial_2\right)h_{,2} = g\left(\frac{1+\alpha}{2}\mathring{W}_{\tau} + \frac{1-\alpha}{2}\mathring{Z}_{\tau} + \frac{\alpha\Sigma}{4\alpha+2}\mathring{S}_{\tau}\right),\tag{3.39a}$$

$$\left(\left(Q + (V - \overline{V})Q_2\right)\partial_s + V\partial_2\right)J_g = \frac{1+\alpha}{2}J_g\mathring{W}_n + \frac{1-\alpha}{2}J_g\mathring{Z}_n + \frac{\alpha\Sigma}{4\alpha+2}J_g\mathring{S}_n,$$
(3.39b)

$$(Q + \overline{V}Q_2)\partial_s h = g^{\frac{1}{2}} \left(\frac{1+\alpha}{2}W + \frac{1-\alpha}{2}Z\right), \tag{3.39c}$$

and the auxiliary quantities  $(\xi, \theta)$  satisfy

$$\partial_s \theta = \frac{1}{Q + \overline{V}Q_2}, \qquad \partial_s \xi = \frac{-\overline{\partial_t J_{g,1}}}{\overline{J_{g,11}}(Q + \overline{V}Q_2)}. \tag{3.40}$$

It follows from (3.38) and remap-aux that

$$\partial_{2}J_{g}(\boldsymbol{x},t) = (1 - Q_{2}V(Q + (V - \overline{V})Q_{2})^{-1})\partial_{2}J_{g}(\boldsymbol{x},s) + Q_{2}(Q + (V - \overline{V})Q_{2})^{-1}(\frac{1+\alpha}{2}J_{g}\mathring{W}_{n} + \frac{1-\alpha}{2}J_{g}\mathring{Z}_{n} + \frac{\alpha\Sigma}{4\alpha+2}J_{g}\mathring{S}_{n})(\boldsymbol{x},s),$$
(3.41a)  
$$\partial_{2}h_{,2}(\boldsymbol{x},t) = (1 - Q_{2}V(Q + (V - \overline{V})Q_{2})^{-1})\partial_{2}h_{,2}(\boldsymbol{x},s) + Q_{2}(Q + (V - \overline{V})Q_{2})^{-1}g(\frac{1+\alpha}{2}\mathring{W}_{\tau} + \frac{1-\alpha}{2}\mathring{Z}_{\tau} + \frac{\alpha\Sigma}{4\alpha+2}\mathring{S}_{\tau})(\boldsymbol{x},s).$$
(3.41b)

We shall make use of the change of variables formulas (3.41) in the computation of  $\mathring{G}_n$  and  $\mathring{G}_{\tau}$ .

- 3.5.4. Initial conditions on s=0. Thanks to (3.28), initial conditions for the classical and differentiated Riemann variables  $(\boldsymbol{W}, J_g \mathring{\boldsymbol{W}}_n, \mathring{\boldsymbol{W}}_\tau)$  and the auxiliary quantities  $(h, J_g, h, 2)$  are identical to the functions at  $t=t_{\rm in}$ , defined in (3.21).
- 3.5.5. The spacetime-remapped DRV-s system of equations. We shall refer to the system of equations (3.37)–(3.40), with the initial conditions (3.21) and (3.32) as the spacetime-remapped DRV-s system of equations. The full set of dependent variables for this system are given by

$$\mathbf{\Pi}(\boldsymbol{x},s) := (W, Z, A, S, h, J_o \mathring{W}_n, J_o \mathring{Z}_n, J_o \mathring{A}_n, J_o \mathring{S}_n, \mathring{W}_{\tau}, \mathring{Z}_{\tau}, \mathring{A}_{\tau}, St, J_o, h, 2, \xi, \theta), \tag{3.42}$$

which is once again split into a differentiated part  $\Pi = (J_g \mathring{W}_n, J_g \mathring{Z}_n, J_g \mathring{A}_n, J_g \mathring{S}_n, \mathring{W}_\tau, \mathring{Z}_\tau, \mathring{A}_\tau, St, J_g, h,_2)$ , and an undifferentiated part  $\Pi = (W, Z, A, S, h, \xi, \theta)$ , which now also includes the auxiliary quantities  $(\xi, \theta)$ .

3.6. Fractional-order expansions of the Euler solution about the "flattened" pre-shock at s=1. We now use the definition (3.34) of the curve of pre-shocks  $\Xi^*$ . Just as in Section 3.4, following [8], [1], and [6], we have the following Puiseux expansions for the solution in Eulerian variables and in (y,s) coordinates, about  $\Xi^*$  at the time s=1: for each  $y_2\in\mathbb{T}$ , the dominant Riemann variable  $w(y_1,y_2,s)$  exhibits a  $C^{\frac{1}{3}}$  cusp at  $y_1=y_1^*(y_2)$  at time s=1, of the form

$$w(y_1, y_2, 1) = c_0^w(y_2) + c_1^w(y_2)(y_1 - y_1^*(y_2))^{\frac{1}{3}} + O(|y_1 - y_1^*(y_2)|^{\frac{2}{3}}),$$
(3.43)

for some functions  $y_2 \mapsto c_i^w(y_2) \in C^4(\mathbb{T})$ , i=0,1. The subdominant Riemann variables  $z(\cdot,y_2,1)$ ,  $a(\cdot,y_2,1)$ ,  $s(\cdot,y_2,1)$  are  $C^{1,\frac{1}{3}}$  functions of the form

$$z(y_1, y_2, 1) = c_0^z(y_2) + c_3^z(y_2)(y_1 - y_1^*(y_2)) + c_4^z(y_2)(y_1 - y_1^*(y_2))^{\frac{4}{3}} + O(|y_1 - y_1^*(y_2)|^{\frac{5}{3}}),$$
(3.44a)

$$a(y_1, y_2, 1) = c_0^a(y_2) + c_3^a(y_2)(y_1 - y_1^*(y_2)) + c_4^a(y_2)(y_1 - y_1^*(y_2))^{\frac{4}{3}} + O(|y_1 - y_1^*(y_2)|^{\frac{5}{3}}),$$
(3.44b)

$$s(y_1, y_2, 1) = c_0^s(y_2) + c_3^s(y_2)(y_1 - y_1^*(y_2)) + c_4^s(y_2)(y_1 - y_1^*(y_2))^{\frac{4}{3}} + O(|y_1 - y_1^*(y_2)|^{\frac{5}{3}}),$$
(3.44c)

for some functions  $c_i^z$ ,  $c_i^a$ ,  $c_i^s \in C^4(\mathbb{T})$ , i = 0, 3, 4. The velocity and sound speed  $(u, \sigma)$  are  $C^{\frac{1}{3}}$  functions of the form

$$u^{1}(y_{1}, y_{2}, 1) = c_{0}^{u1}(y_{2}) + c_{1}^{u1}(y_{2})(y_{1} - y_{1}^{*}(y_{2}))^{\frac{1}{3}} + O(|y_{1} - y_{1}^{*}(y_{2})|^{\frac{2}{3}}),$$
(3.45a)

$$u^{2}(y_{1}, y_{2}, 1) = c_{0}^{u^{2}}(y_{2}) + c_{1}^{u^{2}}(y_{2})(y_{1} - y_{1}^{*}(y_{2}))^{\frac{1}{3}} + O(|y_{1} - y_{1}^{*}(y_{2})|^{\frac{2}{3}}),$$
(3.45b)

$$\sigma(y_1, y_2, 1) = c_0^{\sigma}(y_2) + c_1^{\sigma}(y_2)(y_1 - y_1^*(y_2))^{\frac{1}{3}} + O(|y_1 - y_1^*(y_2)|^{\frac{2}{3}}),$$
(3.45c)

for some functions  $c_i^{u1}, c_i^{u2}, c_i^{\sigma} \in C^4(\mathbb{T}), i=0,1$ . Formulas for the coefficient functions  $c_i^q(y_2)$  as well as the blowup times  $t^*(y_2)$  and the blowup locations  $y_1^*(y_2)$  in terms of the variables  $\Pi(x,s)$  are given in Appendix A.

## 4. A PRECURSOR TO THE COMPUTATIONAL SHOCK FORMATION ALGORITHM

Before we describe our *Computational Shock Formation* (CSD) algorithm, we first present a stable high-order accurate discretization for the Euler equations, intended to numerically compute the solution up to the time of the first singularity. We now describe the numerical method for solving the DRV system (3.15)–(3.18) up to the time of first singularity  $t = T^*$ . The novelty of this scheme is (only) in its use of the DRV system in ALE coordinates with the effect that the collection of variables  $\Pi(x,t)$  in (3.20) remain smooth even up to the first blowup time  $t = T^*$ , leading to high-order convergence properties under mesh refinement. The more innovative CSF algorithm is then presented in Section 5; with the CSF algorithm, we are able to numerically solve the Euler equations in (x, s) past the time of the first singularity, and in fact for times  $s \in [0, 1]$  defined in 3.27, up to the curve of pre-shocks at s = 1.

4.1. Discretization of the DRV system up to time of first singularity. We now describe our numerical method for the DRV system (3.15)–(3.18) up to the time of the first singularity  $T^*$ . We have implemented a fourth order finite-difference scheme in space and MATLAB's ode45 (an adaptive 4th order explicit Runge-Kutta method) in time to numerically approximate equations (3.15)–(3.18), given in vector form by (3.11), for the set of dependent variables  $\Pi$ . We discretize the domain  $\mathbb{T}^2 = [-\pi, \pi] \times [-\pi, \pi]$  using an  $n_1 \times n_2$  grid, so that  $\Delta x_i = 2\pi/n_i$  for i = 1, 2. A function  $F(\boldsymbol{x}, t)$  is discretized on this grid as

$$F_{(i,j)}(t) = F(\mathbf{x}_{(i,j)}, t),$$
  $\mathbf{x}_{(i,j)} = (-\pi + i\Delta x_1, -\pi + j\Delta x_2),$ 

and we define the 4th-order accurate discrete derivative operators by

$$\begin{split} D_1 F_{(i,j)} &= \frac{-25 F_{(i,j)} + 48 F_{(i+1,j)} - 36 F_{(i+2,j)} + 16 F_{(i+3,j)} - 3 F_{(i+4,j)}}{12 \Delta x_1}, \\ D_2 F_{(i,j)} &= \frac{F_{(i,j-2)} - 8 F_{(i,j-1)} + 8 F_{(i,j+1)} - F_{(i,j+2)}}{12 \Delta x_2}, \end{split}$$

where the indices have been periodized so that

$$F_{(n_1+i,j)} = F_{(i,j)},$$
 and  $F_{(i,n_2+j)} = F_{(i,j)}.$ 

Spatially discretizing the vector equations (3.11) yields

$$\frac{d}{dt}\mathbf{W}_{(i,j)} + V_{(i,j)}D_2\mathbf{W}_{(i,j)} + \mathbf{E}_{(i,j)}^1\mathring{\mathbf{W}}_{n,(i,j)} + (\mathbf{E}^{\tau}_{(i,j)} - A_{(i,j)}\mathbf{I})\mathring{\mathbf{W}}_{\tau,(i,j)} = \mathbf{G}_{(i,j)}, \tag{4.1a}$$

$$\frac{d}{dt}(J_g\mathring{\mathbf{W}}_n)_{(i,j)} + \mathbf{E}^1_{(i,j)}D_1\mathring{\mathbf{W}}_{n,(i,j)} + (\mathbf{E}^2_{(i,j)} + V_{(i,j)}\mathbf{I})D_2(J_g\mathring{\mathbf{W}}_n)_{(i,j)} = (J_g\mathring{\mathbf{G}}_n)_{(i,j)}, \tag{4.1b}$$

$$\frac{d}{dt}\mathring{\mathbf{W}}_{\tau,(i,j)} + (J_{g,(i,j)})^{-1}\mathbf{E}_{(i,j)}^{1}D_{1}\mathring{\mathbf{W}}_{\tau,(i,j)} + (\mathbf{E}_{(i,j)}^{2} + V\mathbf{I})(D_{2}\mathring{\mathbf{W}}_{\tau,(i,j)} = \mathring{\mathbf{G}}_{\tau,(i,j)},$$
(4.1c)

and discretizing (3.18) yields

$$\frac{d}{dt}J_{g,(i,j)} + V_{(i,j)}D_2J_{g,(i,j)} = \frac{1+\alpha}{2}(J_g\mathring{W}_n)_{(i,j)} + \frac{1-\alpha}{2}(J_g\mathring{Z}_n)_{(i,j)} + \frac{\alpha\Sigma_{(i,j)}}{4\alpha+2}(J_g\mathring{S}_n)_{(i,j)}, \tag{4.2a}$$

$$\frac{d}{dt}h_{,2,(i,j)} + V_{(i,j)}D_2h_{,2,(i,j)} = \frac{1+\alpha}{2}\mathring{W}_{\tau(i,j)} + \frac{1-\alpha}{2}\mathring{Z}_{\tau(i,j)} + \frac{\alpha\Sigma_{(i,j)}}{4\alpha+2}\mathring{S}_{\tau(i,j)}, \tag{4.2b}$$

$$\frac{d}{dt}h_{(i,j)} = g_{(i,j)}^{\frac{1}{2}} \left( \frac{1+\alpha}{2} W_{(i,j)} + \frac{1-\alpha}{2} Z_{(i,j)} \right) + \alpha \Sigma_{(i,j)} \right). \tag{4.2c}$$

Smooth, locally compressive, and generic initial conditions for the system of ODEs (4.1) and (4.2) are given by the spatial discretization of (3.21):

$$\mathbf{W}_{(i,j)}(0) = \mathbf{w}_0(-\pi + i\Delta x_1, -\pi + j\Delta x_2),$$
 (4.3a)

$$J_{a}\mathring{W}_{n,(i,j)}(0) = \partial_{1}w_{0}(-\pi + i\Delta x_{1}, -\pi + j\Delta x_{2}),$$
 (4.3b)

$$\mathring{\boldsymbol{W}}_{\tau,(i,j)}(0) = \partial_2 \boldsymbol{w}_0(-\pi + i\Delta x_1, -\pi + j\Delta x_2), \qquad (4.3c)$$

$$J_{q,(i,j)}(0) = 1, (4.3d)$$

$$h_{2,(i,j)}(0) = 0,$$
 (4.3e)

$$h_{(i,j)}(0) = -\pi + i\Delta x, \qquad (4.3f)$$

where  $\mathbf{w}_0 = (z_0, a_0, w_0, s_0)^T$ .

**Definition 4.1** (The DRV- $N_1$ - $N_2$  numerical simulation). The numerical solution of the initial value problem (4.1)–(4.3) is called the DRV- $N_1$ - $N_2$  solution for integers  $N_1$ ,  $N_2 \ge 4$ , or simply DRV- $N^2$  if  $N_1 = N_2 = N$ .

Due to the smoothness of solutions to the DRV system, we will demonstrate that the DRV- $n_1$ - $n_2$  solutions converge uniformly with 4th-order accuracy as  $\Delta x := (\Delta x_1, \Delta x_2) \to 0$ .

4.2. Numerical solution on the time interval  $[0, T^*]$ . The time-step in our explicit Runge-Kutta is subject to the CFL condition and satisfies the following bound

$$\Delta t \left( \frac{2\alpha \|\Sigma\|_{\infty}}{J_g \Delta x_1} + \frac{\|V + 2\alpha \Sigma g^{-\frac{1}{2}} h_{,2}\|_{\infty}}{\Delta x_2} \right) \le \text{CFL}, \tag{4.4}$$

where  $0 < \mathrm{CFL} \le 1$ . We will set  $\mathrm{CFL} = 1$  in our simulations. Since  $V, \Sigma, g^{-\frac{1}{2}}$ , and h, 2 remain uniformly bounded for  $t \in [\mathsf{t_{in}}, T^*]$ , it is the fact that  $J_g(\boldsymbol{x}^*, t) \to 0$  as  $t \to T^*$  that limits the size of the time-step for times close to the first blowup time. This means that we must approximate the vanishing condition  $J_g(\boldsymbol{x}^*, T^*) = 0$  with an approximation. We have the following

**Definition 4.2** (The numerically-computed time of first singularity  $t = T_{\text{num}}^*$ ). We set

$$J_* = \Delta x_1^4. \tag{4.5}$$

When employing a DRV- $N^2$  simulation, we let  $T^*_{num}(N)$  denote the numerically-computed time of first singularity by requiring that

$$\min_{(i,j)} J_{g(i,j)}(T_{\text{num}}^*) = J_*. \tag{4.6}$$

The condition (4.6) is our discrete approximation for continuum condition  $J_g(\mathbf{x}^*, T^*) = 0$ , and we say that computational shock formation occurs when (4.6) is satisfied.

**Definition 4.3** (Numerically computed blowup label and blowup location at  $t = T_{\text{num}}^*$ ). Once the DRV- $N^2$  solution at the numerically computed time of first singularity  $t = T_{\text{num}}^*$  is known, we define the numerically computed blowup label by

$$oldsymbol{x}^*_{\mathrm{num}}(N) = oldsymbol{x}_{(i^*,j^*)}, \qquad \textit{where} \qquad (i^*,j^*) = \operatornamewithlimits{argmin}_{(i,j)} J_{g,(i,j)}(T^*_{\mathrm{num}})(N)$$

<sup>&</sup>lt;sup>5</sup>By setting  $J_* = \Delta x_1^4$ , we can maintain 4th-order accuracy of our numerical method on the time interval  $[0, T_{\text{num}}^*]$ . It is, however, possible to define  $J_* = \Delta x^k$ , for  $k \in \{1, 2, 3\}$ , in which case the scheme reduces to kth-order accuracy on the time interval  $[0, T_{\text{num}}^*]$ . This may be beneficial for simulations in which the 4th-order condition requires a prohibitively small CFL condition.

and the numerically computed blowup location at the time of first singularity is given as

$$\mathbf{y}_{\text{num}}^*(N) = \left(h_{(i^*,j^*)}(T_{\text{num}}^*(N)), x_{2(i^*,j^*)}(N)\right).$$

4.3. A periodic reference solution. In order to demonstrate 4th-order convergence of the DRV- $N^2$  solutions we shall define a resolved periodic reference solution which evolves initial conditions satisfying Definition 2.1.

**Definition 4.4** (Periodic Reference Solution). *Consider the following locally compressive and generic initial conditions set at the initial time*  $t_{in} = 0$ :

$$w_0(\mathbf{x}) = \kappa_0 - \sin\left(\frac{x_1}{\varepsilon}\right) \left(1 - \delta + \delta \cos(x_2)\right),\tag{4.7a}$$

$$z_0(\mathbf{x}) = -\beta \cos\left(\frac{x_1}{\varepsilon}\right),\tag{4.7b}$$

$$a_0(\mathbf{x}) = -\beta \cos\left(\frac{x_1}{\varepsilon}\right),$$
 (4.7c)

$$s_0(\mathbf{x}) = \beta \sin\left(\frac{x_1}{\varepsilon}\right),\tag{4.7d}$$

where  $\kappa_0=2$ ,  $\varepsilon=\frac{1}{4}$ ,  $\delta=\frac{1}{5}$ , and  $\beta=\frac{1}{20}$ . For the purpose of convergence studies, the DRV-512<sup>2</sup> solution, which uses the initial conditions (4.7), is called the reference solution. The adiabatic exponent in (2.1) is set to  $\alpha=\frac{1}{5}$ . For this data, we identify  $\mathbb{T}^2$  with the periodic box  $[-\frac{\pi}{4},\frac{\pi}{4}]\times[-\pi,\pi]$ .

**Definition 4.5** (Notation for the discretized Euler solution using the DRV variables  $\Pi$ ). With the nodal locations  $x_{(i,j)}$  of the numerical mesh parameterized by (i,j) for i=1,...,N and j=1,...,N, we denote the DRV- $N^2$  solution by  $\Pi_{(i,j)}^N(t)$  for  $t\in[\mathsf{t}_{\mathsf{in}},T^*_{\mathsf{num}}]$  and we denote the exact solution by  $\Pi(x_{(i,j)})(t)$ .

**Definition 4.6** (The  $L^{\infty}$  error). For integers  $M, N \geq 4$  and  $t \in [t_{in}, T_{num}^*]$ , we set

$$\left\|\mathbf{\Pi}^{N}(t)-\mathbf{\Pi}^{M}(t)\right\|_{L^{\infty}}=\sup_{i,j}\left|\mathbf{\Pi}_{(i,j)}^{N}(t)-\mathbf{\Pi}_{(i,j)}^{M}(t)\right|,$$

and

$$\left\|\mathbf{\Pi}^{N}(t) - \mathbf{\Pi}(t)\right\|_{L^{\infty}} = \sup_{i,j} \left|\mathbf{\Pi}_{(i,j)}^{N}(t) - \mathbf{\Pi}(\boldsymbol{x}_{(i,j)})(t)\right|.$$

4.4. 4th-order accurate convergence for the  $L^{\infty}$  error. We have computed that

$$T_{\text{num}}^*(512) = 0.416306 \text{ and } \boldsymbol{y}_{\text{num}}^*(512) = (0.494098, -0.012271)$$

for the periodic reference solution. Using the periodic initial conditions and parameters in Definition (4.4), for  $\Delta x_1 = \frac{\pi}{2N}$  and  $\Delta x_2 = \frac{2\pi}{N}$ , Figure 4 shows the 4th-order convergence

$$|T_{\text{num}}^*(N) - T_{\text{num}}^*(512)| = O(|\Delta x|^4) \text{ as } |\Delta x| \to 0.$$

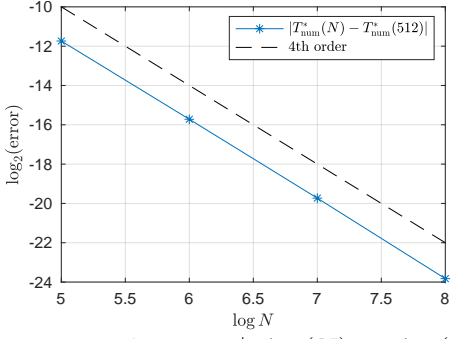


FIGURE 4. Displayed is a log-log plot of the error  $|T_{\text{num}}^*(N) - T_{\text{num}}^*(512)|$  with N = 32, 64, 128, 256.

With  $J_*$  defined by (4.5), the DRV- $N^2$  solutions using the periodic initial conditions (4.7) (and the same parameters as for the periodic reference solution) display 4th-order accurate convergence towards the periodic reference solution. In particular, as shown in Figure 5, we have that for  $\Delta x_1 = \frac{\pi}{2N}$  and  $\Delta x_2 = \frac{2\pi}{N}$ ,

$$\|\boldsymbol{\Pi}^N(T^*_{\mathrm{num}}) - \boldsymbol{\Pi}^{512}(T^*_{\mathrm{num}})\|_{L^\infty} = O(|\boldsymbol{\Delta}\boldsymbol{x}|^4) \text{ as } |\boldsymbol{\Delta}\boldsymbol{x}| \to 0 \,.$$

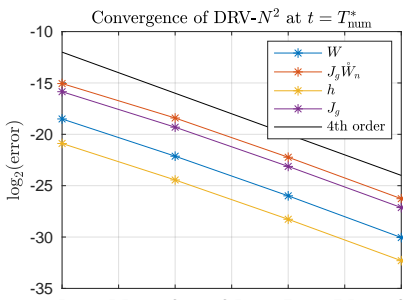


FIGURE 5. Displayed is a log-log plot of  $\|\mathbf{\Pi}^{N}(T_{\text{lng,n}}^{*6.5})^{-7}\mathbf{\Pi}^{5}\|_{L^{\infty}}^{6}$  with N=32,64,128,256.

While only convergence for the variables  $(W,J_g\mathring{W}_n,J_g,h)$  is displayed, all components of  $\Pi^N$  converge with 4th-order accuracy. Note also in Figure 5 that the undifferentiated quantities W and h, have much smaller  $L^\infty$  error than the differentiated quantities  $J_g\mathring{W}_n$  and  $J_g$ .

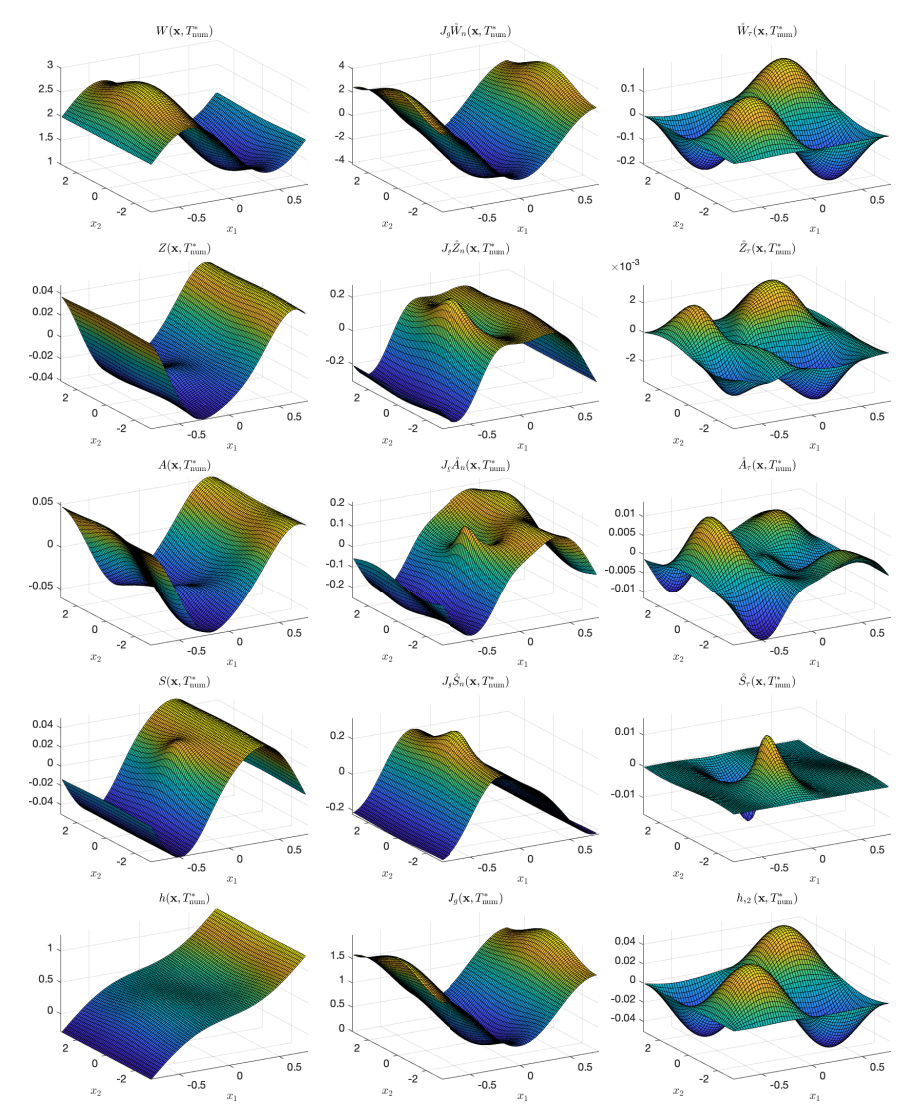


FIGURE 6. Surface plots of the DRV variables in ALE coordinates at the numerically computed time for first singularity  $t=T_{\mathrm{num}}^*$ . All of these variables remain smooth and bounded.

4.5. **Results from a DRV-** $64^2$  **simulation.** We present results of a DRV- $64^2$  simulation using the periodic initial conditions and parameters given in Definition 4.4 and the numerically-computed time of first singularity  $T^*_{\text{num}}(64) = 0.0.416253$ . In Figure 6, we display the surface plots of all components of  $\Pi^{64}(T^*_{\text{num}})$ , which numerically demonstrate regularity assertions of Theorem 4.6 in [8], showing that smoothness is maintained for all components of  $\Pi$ , even at the time of the first singularity  $t = T^*_{\text{num}}$ . Moreover, our simulation demonstrates the bounds of Lemma 6.1 in [8] which suggest that both  $\|W - w_0\|_{L^{\infty}}$  and  $\|J_g\mathring{W}_n - \partial_1 w_0\|_{L^{\infty}}$  are small and bounded by the inverse of the maximal negative slope of the dominant Riemann variable  $w_0$ . In particular, modulo such small error, the both W and  $J_g\mathring{W}_n$  are "almost frozen" into the ALE flow which is adapted to the fast acoustic characteristic surfaces.

In Figure 7, we display a color contour plot of the Eulerian dominant Riemann variable  $w(\boldsymbol{y},t)$  which is overlaid by the mesh deformation by our ALE map  $\psi(\cdot,t)$  of an initially perfectly rectangular grid. Contours of  $w(\boldsymbol{y},t)$  are shown at times (left)  $t=\mathsf{t}_{\mathsf{in}}=0$ , (middle)  $t=\frac{1}{2}T_{\mathsf{num}}^*$ , and (right)  $t=T_{\mathsf{num}}^*$ , where  $T_{\mathsf{num}}^*=T_{\mathsf{num}}^*(64)=0.4171$ . The mesh impingement at  $t=T_{\mathsf{num}}^*$  indicates that the distance between fast acoustic characteristics has vanished at the blowup location  $\boldsymbol{y}_{\mathsf{num}}^*(64)=(0.494163,0)$ . Note the similarity in the color contours at the different instances

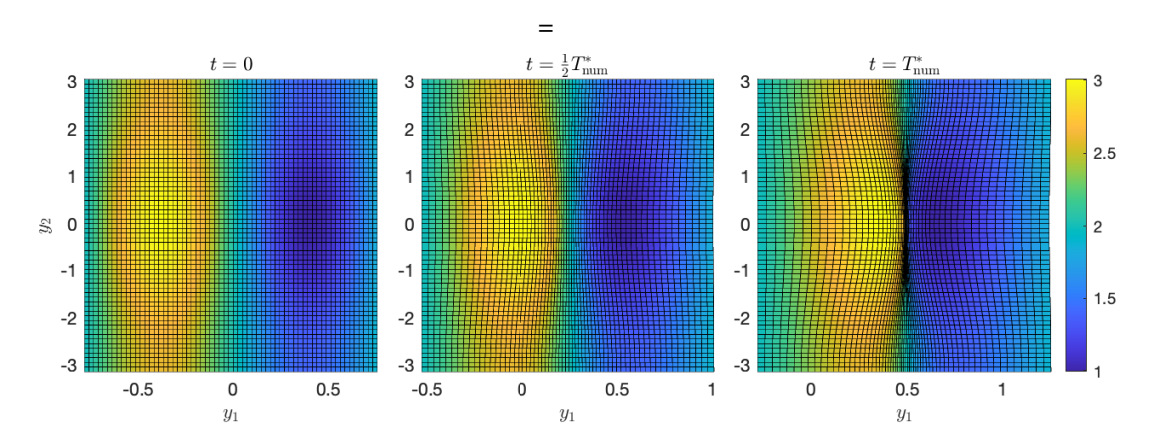


FIGURE 7. Contours of the dominant Riemann variable  $w(\boldsymbol{y},t)$  in Eulerian coordinates computed with a DRV- $64^2$  simulation, overlaid with rectangular mesh deformation by the ALE map  $\psi(\cdot,t)$ , shown at times t=0,  $t=\frac{1}{2}T_{\text{num}}^*$ , and  $t=T_{\text{num}}^*$ .

of time, indicating once again that W is almost frozen into the ALE flow. In fact, we have computed that for this DRV- $64^2$  run, we have that

$$||W - w_0||_{L^{\infty}} = 0.023,$$
  $||J_g \mathring{W}_n - \partial_1 w_0||_{L^{\infty}} = 0.017.$  (4.8)

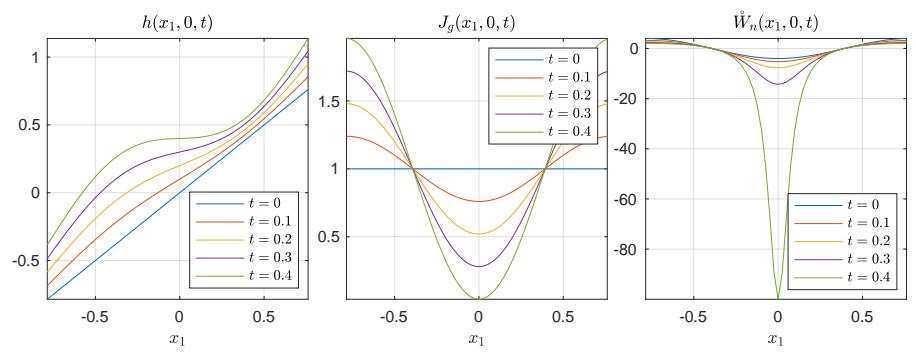


FIGURE 8. Evolution of the height function h, the Jacobian  $J_g$ , and the differentiated Riemann variable  $\mathring{W}_n$  at the cross section  $x_2 = 0$ , shown at times t = 0, 0.1, 0.2, 0.3, 0.4.

Figure 8 shows the evolution of the height function h (left), the metric-scaled Jacobian determinant  $J_g$  (middle), and the differentiated Riemann variable  $\mathring{W}_n$  (right) at five different times and along the cross section  $x_2 = 0$ . At the latest time displayed t = 0.4 is very nearly the time of the first singularity when  $J_g$  has first decreased to the value  $J_*$ .

At this time, the graph of  $\mathring{W}_n(\cdot,0,0.4)$  is an approximation to the infinite magnitude achieved by the exact solution  $\mathring{W}_n$  at  $t=T^*$ .

The results displayed in Figures 6–8 demonstrate a key feature of our numerical method; namely, we have replaced the Eulerian gradient blowup criterion for shock formation by the ALE variant in which shock formation occurs when  $J_g$  vanishes, and all variables remain smooth and bounded. The DRV discretization creates a stable, 4th-order accurate scheme, replacing the usual numerical challenges associated to traditional Eulerian blowup with the comparatively mild difficulty of a small CFL number, as defined in (4.4).

Figure 9 displays a few of the basic variables for the formation of a shock at the final time  $t=T^*_{\rm num}$ , namely the ALE map  $\psi$ , the dominant Riemann variable w, the Jacobian  $J_g$ , and the differentiated Riemann variable  $\mathring{W}_n$ . In particular, it is the image of  $\Psi(\boldsymbol{x},s^*)$  which is displayed in the top left panel and which demonstrates the compression of the fast acoustic wavefronts near the point of the first singularity. In the top right panel of this figure, the Eulerian dominant Riemann variable  $w(\boldsymbol{y},T^*_{\rm num})$  is seen to remain continuous but w does form a  $C^{\frac{1}{3}}$  cusp at  $\boldsymbol{y}=\boldsymbol{y}^*_{\rm num}$  (the numerically computed location of the first singularity). The bottom left panel shows a surface plot of  $J_g(\boldsymbol{x},T^*_{\rm num})$ ; the minimum value of this smooth function occurs at the numerically computed blowup label  $\boldsymbol{x}^*_{\rm num}$  with value  $J_*$ . Finally, in the bottom right panel, we present a surface plot of  $\mathring{W}_n(\boldsymbol{x},T^*_{\rm num})$ . Note that for the exact solution  $\mathring{W}_n(\boldsymbol{x}^*,T^*)=-\infty$ , but as we stop the simulation at  $t=T^*_{\rm num}$  at which time  $J_g$  has the minimal value of  $J_*$ , the graph of the numerically computed  $\mathring{W}_n$  has a very large (but finite) negative value, and resembles an approximation of the Dirac distribution.

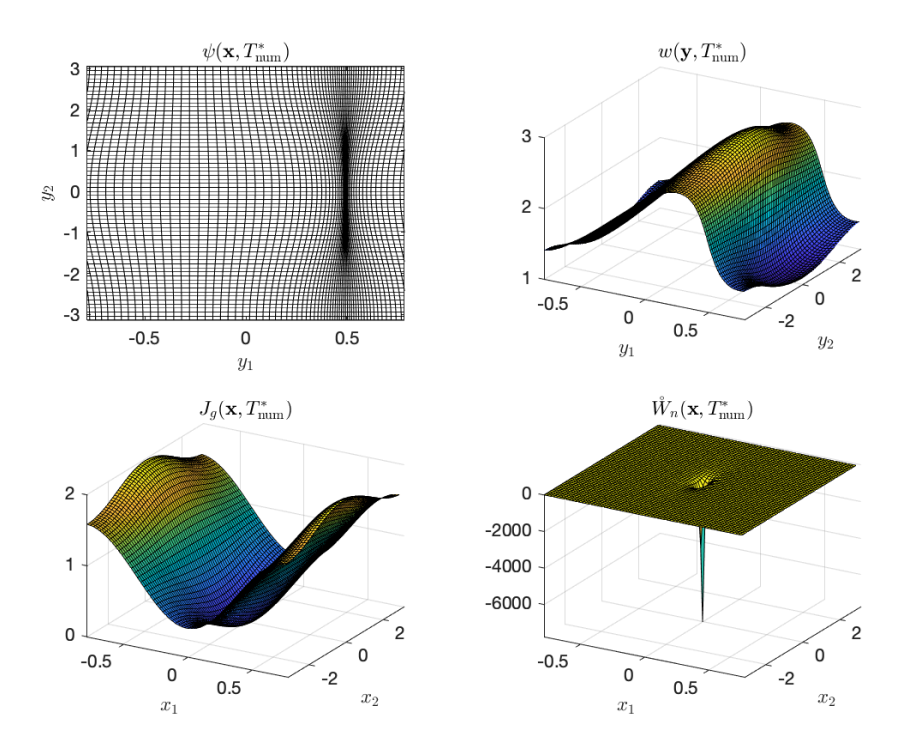


FIGURE 9. DRV- $64^2$  solution at the numerically computed time of first singularity  $T^*_{\rm num}$ , showing the mesh deformation of the ALE map  $\psi$  (top left), the Eulerian Riemann dominant variable w (top right), the metric-scaled Jacobian determinant  $J_g$  (bottom left), and the differentiated Riemann variable  $\mathring{W}_n$  (bottom right).

4.6. Computational complexity of the DRV system. The 4th-order central-differencing that we have employed requires  $O(N_1N_2)$  floating-point operations at each time-step for a mesh with  $N_1 \times N_2$  grid points. Following (4.153) in [1], for  $x^*$  denoting the blowup label, we have that for initial data satisfying Definition 2.1,

$$\frac{2}{1+\alpha} \frac{1-\varepsilon^{\frac{1}{2}}}{\varepsilon} (T^* - t) \le J_g(\boldsymbol{x}^*, t) \le \frac{2}{1+\alpha} \frac{1+\varepsilon^{\frac{1}{2}}}{\varepsilon} (T^* - t). \tag{4.9}$$

From the CFL condition (4.4) and (4.9), there exists a constant  $c_1 > 0$  such that

$$\frac{1}{T^* - t} \frac{1}{\Delta x_1} + \frac{1}{\Delta x_2} \le \frac{\mathsf{c}_1}{\Delta t(t)} \,, \tag{4.10}$$

where the time-step  $\Delta t$  is getting smaller as a function of time t, and by (4.6), we have that  $T_{\text{num}}^* = T^* - \mathsf{c}_2 J_*$  for a constant  $\mathsf{c}_2$  that depends on  $\varepsilon$ . If we define the K discrete values of time by  $\{t_k\}_{k=1}^K$  where  $t_1 = \mathsf{t}_{\text{in}}$  and  $t_K = T_{\text{num}}^* = T^* - \mathsf{c}_2 J_*$ , by setting  $t = t_k$  in (4.10), we see that a lower bound for the the number of time-steps K required to reach  $t = T_{\text{num}}^*$  can be obtained by integrating (4.10) from  $t = \mathsf{t}_{\text{in}}$  to  $t = T^* - \mathsf{c}_2 J_*$ . Using that  $N_1 = \frac{\pi}{2\Delta x_1}$ ,  $N_2 = \frac{2\pi}{\Delta x_2}$ , and  $J_* = \Delta x_1^4$ , this integration shows that  $K = O(N_1 \log(N_1) + N_2)$  as the mesh size tends to zero, and hence the computational complexity of the algorithm up to the time of the first singularity is given by

$$O(N_1 N_2 (N_1 \log(N_1) + N_2)) \tag{4.11}$$

as the mesh size tends to zero. In the case of a non-degenerate PDE, in which  $\Delta t$  scales uniformly with  $|\Delta x|$ , the "standard" computational complexity is  $O(N_1N_2(N_1+N_2))$ . We see that the degeneracy, caused by the vanishing of  $J_g$  at shock formation, creates only a mild logarithmic correction which follows directly from the linear-in-time behavior of  $J_g(x^*,t)$  in (4.9).

4.7. Convergence of the fractional-order expansion coefficients. The coefficients in the fractional-order expansions (3.22) are numerically computed using DRV- $N^2$  solution by the formulae (A.1a) and (A.1b), using 4th-order accurate finite difference approximations for the  $x_1$ -derivatives. The exact formulas, as well as the finite difference stencils utilized, are given in Appendix A.

For the DRV- $64^2$  solution, once again employing the initial conditions and parameters in Definition 4.4, we compute the blowup location  $y_{\text{num}}^* = \text{and } T_{\text{num}}^* = \text{.}$  In the top left panel of Figure 10, we compare DRV- $64^2$  solution for the Eulerian dominant Riemann variable  $w(\cdot, y_{2,\text{num}}^*, T_{\text{num}}^*)$  against the  $C^{\frac{1}{3}}$  function in the expansion (3.22a) about  $y_1 = y_{1,\text{num}}^*$  at  $y_2 = y_{2,\text{num}}^*$ . The comparison shows that even at low resolution, the DRV- $64^2$  solution accurately captures the  $C^{\frac{1}{3}}$  cusp structure at the numerically computed blowup time  $t = T_{\text{num}}^*$ .

The remaining panels in Figure 10 respectively display the comparison between  $(z_{,1}, a_{,1}, s_{,1})$  and the functions

$$c_3^z + \frac{4}{3}c_4^z(y_1 - y_{1,\text{num}}^*)^{\frac{1}{3}}, \qquad c_3^a + \frac{4}{3}c_4^a(y_1 - y_{1,\text{num}}^*)^{\frac{1}{3}}, \qquad c_3^s + \frac{4}{3}c_4^s(y_1 - y_{1,\text{num}}^*)^{\frac{1}{3}},$$

which are the formally computed 1-derivatives of the fractional-order expansions (3.22b), (3.22c), and (3.22d). (See [6] for a justification of such differentiation formulas.)

4.8. Convergence of DRV- $N^2$  for a plane wave Burgers solution. We now verify that the numerically computed values of the time  $T^*_{\text{num}}$  of first singularity, the blowup location  $y^*_{\text{num}}$  at the time of first singularity, and the singular expansion coefficient  $c^w_{1,\text{num}}$  in (3.22a), each computed from a DRV- $N^2$  solution, converge to the exact values as  $N \to \infty$ .

By choosing the initial conditions at time  $t_{in} = 0$  for which only the dominant Riemann variable  $w_0$  is non-trivial and depends only the  $x_1$  coordinate,

$$w_0(x_1) = 2 - \sin\left(\frac{x_1}{\varepsilon}\right), \qquad z_0(x) = 0, \qquad a_0(x) = 0, \qquad s_0(x) = 0,$$
 (4.12)

with  $\varepsilon=\frac{1}{4}$ , the DRV system (3.15)–(3.18) simplifies to the one-dimensional Burgers equation,  $\partial_t w+\frac{1+\alpha}{2}w\partial_1 w=0$ , which has the closed-form solution:

$$w(x_1 - \frac{1+\alpha}{2}tw_0(x_1), t) = w_0(x_1), \ x_1 \in \mathbb{T}, \ t \in [0, T^*], \ \alpha = \frac{1}{5},$$
 (4.13)

where  $T^*=\frac{5}{12},$   $y_1^*=\frac{1}{2},$  and the fractional-order expansion of  $w(y_1,T^*)$  about  $y_1^*=\frac{1}{2}$  is given by

$$w_0(y_1, \frac{5}{12}) = 2 + c_1^w(y_1 - \frac{1}{2})^{\frac{1}{3}} + O(|y_1 - \frac{1}{2}|^{\frac{2}{3}}).$$
(4.14)

where  $c_1^w = -2^{\frac{2}{3}}$ .

Using the initial data (4.12), we show that our DRV- $N^2$  solutions converge with 4th-order accuracy to the exact solution (4.13) and the Puiseux expansion (4.14). For these simulations, we identity  $\mathbb{T}^2$  with the periodic box  $\left[-\frac{\pi}{2}, \frac{\pi}{2}\right] \times \left[-\pi, \pi\right]$ .

Figure 11 shows a log-log plot of the errors

$$|c_{1 \text{ num}}^{w}(N) - c_{1}^{w}|, \qquad |y_{1 \text{ num}}^{*}(N) - y_{1}^{*}|, \qquad |T_{\text{num}}^{*}(N) - T^{*}|,$$

demonstrating the 4th-order convergence of these quantities as  $N \to \infty$  or equivalently as  $|\Delta x| \to 0$ . We note that our numerical computation of  $T^*_{\text{num}}(N)$  is computed with machine precision. For this solution, we can compute the

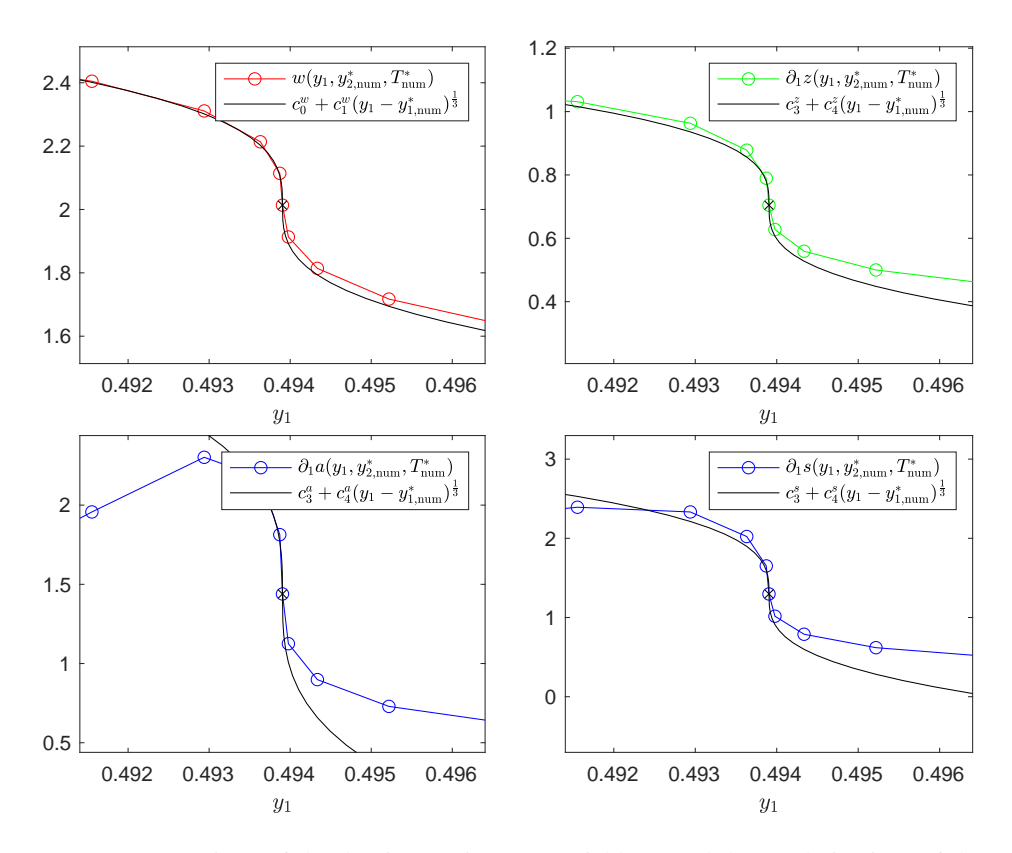


FIGURE 10. Comparison of the dominant Riemann variable w and the  $x_1$ -derivatives of the sub-dominant Riemann variables,  $(z,_1,a,_1,s,_1)$ , computed from the DRV- $64^2$  solution, compared against their  $C^{\frac{1}{3}}$  fractional-order expansions, zoomed in near the blowup location  $y^*$ .

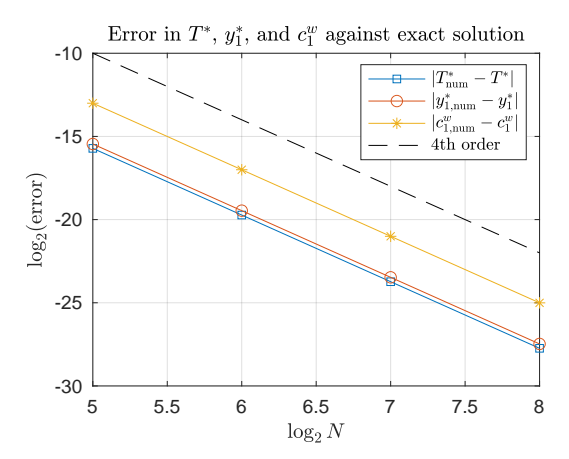


FIGURE 11. (Left) 4th-order accurate convergence of the numerically computed fractional-order expansion coefficient  $c_{1,\text{num}}^w$ , the blowup location  $y_{\text{num}}^*$ , and the blowup time  $T_{\text{num}}^*$  to the exact solution (4.13).

exact value of  $T^*_{\mathrm{num}}(N_1)$  to be  $T^* - \frac{2\varepsilon}{(1+\alpha)}J_* = \frac{5}{12} - \frac{5}{12}\Delta x_1^4$ . In particular, we have that  $|T^*_{\mathrm{num}}(N_1) - \frac{5}{12} - \frac{5}{12}\Delta x_1^4| = 1.69 \times 10^{-10}, 1.89 \times 10^{-11}, 3.66 \times 10^{-13}$  for  $N_1 = 128, 256, 512$ , respectively.

The value of  $T_{\mathrm{num}}^*$  is computed using the Events subroutine in the MATLAB ODE solver ode45. This subroutine employs a root-finding algorithm to cease integration when the minimum value of  $J_{g,(i,j)}$  is equal to  $J_*$ . To compute

the blowup location  $oldsymbol{x}^*_{ ext{num}}$ , we numerically solve the ODE

$$rac{d}{dt}oldsymbol{x}^*(t) = -ig(D^2J_g(oldsymbol{x}^*(t),t)ig)^{-1}\partial_toldsymbol{
abla}J_g(oldsymbol{x}^*(t),t)\,,\;\;t>\mathsf{t}_{\mathsf{in}}\,,$$

where  $D^2J_g$  means the 2×2 Hessian matrix of  $J_g$  and  $\nabla$  denotes the spatial gradient  $(\partial_1, \partial_2)$ . The fact that follows from Corollary 6.2 and inequality (6.24e) in [8], together with the "genericity" condition  $\nabla^2\partial_1w_0(0)\geq \frac{1}{\varepsilon^3}\mathrm{Id}$  stipulated in Definition 2.1. The ODE for  $\boldsymbol{x}^*(t)$  is supplemented with the initial condition

$$m{x}^*(\mathsf{t}_\mathsf{in}) = \operatorname*{argmin}_{m{x} \in \mathbb{T}^2} \left( \frac{1+lpha}{2} \partial_1 w_0(m{x}) + \frac{1-lpha}{2} \partial_1 z_0(m{x}) \right).$$

We then define

$$\boldsymbol{x}_{\mathrm{num}}^* := \boldsymbol{x}^*(T_{\mathrm{num}}^*)$$
.

We note that in using MATLAB to solve the ODE for  $\boldsymbol{x}^*(t)$ , the derivatives of  $J_g$  are evaluated at  $\boldsymbol{x} = \boldsymbol{x}^*(t)$  using MATLAB 2D function interp2 with cubic interpolation; then,  $\boldsymbol{y}_{\text{num}}^* = h(\boldsymbol{x}_{\text{num}}^*, T_{\text{num}}^*)$  is computed by once again using the MATLAB function interp2. For the reference initial data (4.7), we have that

$$m{x}^*_{\mathrm{num}}(64) = (-0.001702, -0.023757) \text{ and } m{y}^*_{\mathrm{num}}(64) = (0.493902, -0.023757)$$
 ,

while

$$m{x}^*_{\mathrm{num}}(512) = (-0.001702, -0.023749)$$
 and  $m{y}^*_{\mathrm{num}}(512) = (0.494080, -0.023757)$  .

The singular expansion coefficients, which are given in Appendix A in terms of the dependent variables  $\Pi(x_{\text{num}}^*, T_{\text{num}}^*)$ , are also computed using the MATLAB function interp2.

### 5. THE COMPUTATIONAL SHOCK FORMATION ALGORITHM

We now present our computational shock formation algorithm, which provides the numerical solution to the Euler equations in (x, s)-coordinates, past the time of the first singularity, and in fact for times  $s \in [0, 1]$  defined in 3.27, up to the curve of pre-shocks at s = 1.

The variables  $\Pi(x, s)$  in (3.42) used in our DRV-s system remain smooth up to the entire curve of pre-shocks at s=1. Our numerical discretization, using 4th-order central differencing operators in space and MATLAB's ode45 Runge-Kutta explicit time-stepping, produces 4th-order accuracy for the numerically computed Euler solution up to and including the curve of pre-shocks  $\Xi^*$ . Moreover, our CSF algorithm can compute with 4th-order accuracy the fractional-order expansions (3.43) for w and (3.44) for (z, a, s) about the entire curve of pre-shocks at s=1, which is an essential ingredient for the problem of computational shock development (see, for example, Section 3 of [7]).

For a numerical scheme to maintain high-order accuracy up to the curve of pre-shocks  $\Xi^*$ , it is necessary to employ

- (a) a system of variables and coordinates that remain smooth, even as the Euler solutions experiences a continuum of Eulerian gradient singularities, and
- (b) a smooth and invertible spacetime remapping that flattens the pre-shock cylindrical future temporal boundary. Our CSF algorithm employs the DRV functions in adapted ALE coordinates to satisfy (a) and makes use of the new time coordinate s, defined in (3.27), to satisfy (b). To our knowledge, this CSF algorithm is the first high-order scheme that is capable of accurately determining the spacetime location of the pre-shock curve as well as the fractional-order expansion of the Euler solution about this pre-shock set.
- 5.1. **Discretizing the DRV-**s **system.** We describe our CSF algorithm for solving the DRV-s system using the temporal remapping (3.27), which enables us to compute the fractional-order expansions of the Riemann variables (w, z, a, s) along the full curve of pre-shocks  $\Xi^*$ .
- 5.1.1. The discretized CSF algorithm using DRV-s. Spatial derivatives are once again discretized using 4th order centered differences, and time-stepping is achieved using MATLAB's ode45 routine. We recall that the variables with the overline symbol,  $\overline{V}$  and  $\overline{J}_{g,2}$ , denote evaluation at along the surface  $x_1 = \xi(x_2, s)$ , and are computed at each time-step via MATLAB's cubic-interpolation function interp1. The semi-discrete version of the DRV-s system of Euler equations (3.37) takes the form

$$\frac{d}{ds}\mathbf{W}_{(i,j)} = Q_j^{-1} (\mathbf{G}_{(i,j)} - V_{(i,j)} D_2 \mathbf{W}_{(i,j)} - \mathbf{E}_{(i,j)}^1 \mathring{\mathbf{W}}_{n,(i,j)} - (\mathbf{E}_{(i,j)}^{\tau} - A_{(i,j)} \mathbf{I}) \mathring{\mathbf{W}}_{\tau,(i,j)}),$$
(5.1a)

$$\frac{d}{ds}(J_g \mathring{\mathbf{W}}_n)_{(i,j)} = \mathbf{M}_{(i,j)}^{-1} \left( (J_g \mathring{\mathbf{G}}_n)_{(i,j)} - \mathbf{E}_{(i,j)}^1 D_1 \mathring{\mathbf{W}}_{n,(i,j)} - (\mathbf{E}_{(i,j)}^2 + V_{(i,j)} \mathbf{I}) D_2 (J_g \mathring{\mathbf{W}}_n)_{(i,j)} \right), \tag{5.1b}$$

$$\frac{d}{ds} \mathring{\mathbf{W}}_{\tau,(i,j)} = \mathbf{M}_{(i,j)}^{-1} \left( \mathring{\mathbf{G}}_{\tau,(i,j)} - J_{g,(i,j)}^{-1} \mathbf{E}_{(i,j)}^{1} D_{1} \mathring{\mathbf{W}}_{\tau,(i,j)} - (\mathbf{E}_{(i,j)}^{2} + V_{(i,j)} \mathbf{I}) D_{2} \mathring{\mathbf{W}}_{\tau,(i,j)} \right), \tag{5.1c}$$

and the semi-discrete version of the evolution of geometric quanties (3.39) is written as

$$\frac{d}{ds}h_{,2,(i,j)} = Q_j^{-1} \left( -V_{(i,j)} D_2 h_{,2,(i,j)} + \frac{1+\alpha}{2} \mathring{W}_{\tau(i,j)} + \frac{1-\alpha}{2} \mathring{Z}_{\tau(i,j)} + \frac{\alpha \Sigma_{(i,j)}}{4\alpha + 2} \mathring{S}_{\tau(i,j)} \right), \tag{5.2a}$$

$$\frac{d}{ds}J_{g,(i,j)} = Q_j^{-1} \left( -V_{(i,j)}D_2J_{g,(i,j)} + \frac{1+\alpha}{2}(J_g\mathring{W}_n)_{(i,j)} + \frac{1-\alpha}{2}(J_g\mathring{Z}_n)_{(i,j)} + \frac{\alpha\Sigma_{(i,j)}}{4\alpha+2}(J_g\mathring{S}_n)_{(i,j)} \right), \tag{5.2b}$$

$$\frac{d}{ds}h_{(i,j)} = \left(Q_j + \overline{V}_j(j)Q_{2,j}\right)^{-1}g_{(i,j)}^{\frac{1}{2}}\left(\frac{1}{2}(W_{(i,j)} + Z_{(i,j)}) + \alpha\Sigma_{(i,j)}\right). \tag{5.2c}$$

We must additionally consider the semi-discrete form of the equations for  $\theta(x_2, s)$  and  $\xi(x_2, s)$  given in (3.40) as

$$\frac{d}{ds}\theta_j = \frac{1}{Q_j + \overline{V}_j Q_{2,j}}, \qquad \frac{d}{ds}\xi_j = \frac{-(\overline{D}_1 \partial_t J_g)_j}{\overline{J}_g(j)(Q_j + \overline{V}_j Q_{2,j})}.$$
(5.3)

We note that our numerical solution for the ordinary differential equations in (5.3) employs the cubic interpolation MATLAB function interp1 for the evaluations of the *overlined* quantities.

Recall that  $\theta$  maps the time coordinate s back to the original time t, and that according to (3.3),  $y_2 = \psi_2(x,t) = x_2$  so that  $\theta(y_2,s) = \theta(x_2,s)$ . In the left panel of Figure 12, we display a foliation of the spacetime  $\Omega^*$  by the surfaces  $\theta(y_2,s)$  for eight different values of s and we display as the red curve the Eulerian pre-shock set

$$(h(\xi(x_2,1), x_2, \theta(x_2,1)), x_2, \theta(x_2,1)). \tag{5.4}$$

The right panel of Figure 12 shows the foliation of the Eulerian spacetime by the fast acoustic characteristic surfaces

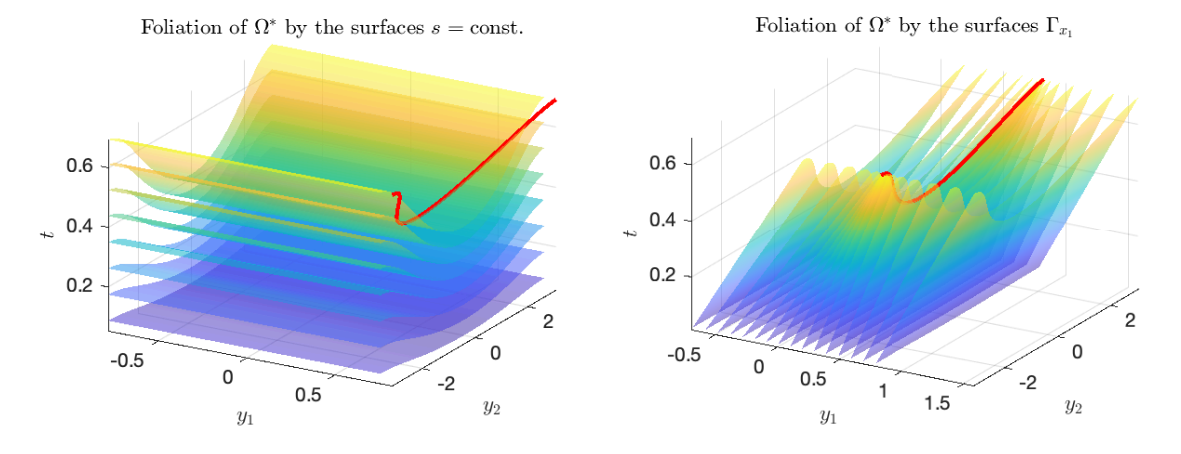


FIGURE 12. (Left). On display, is the foliation of  $\Omega^*$  by  $\theta(y_2, s)$  for 8 values of s together with the Eulerian curve of pre-shocks (red). (Right). Foliation of the Eulerian spacetime by a discrete set of fast acoustic characteristic surfaces.

with the same pre-shock curve as is displayed in the left panel. The initial conditions and parameters from Definition 4.4 have been used. This fast characteristic surfaces are evolved up to the future temporal boundary of the spacetime  $\Omega^*$ . This should be compared with the left panel in Figure 1 in which the fast characteristic surfaces continue beyond the pre-shock curve and capture the  $\overline{\text{MGHD}}$ .

5.1.2. Initial conditions for CSF using DRV-s. Initial data is specified along the initial time-slice  $\{s=0\}$  which coincides with the time-slice  $t=t_{\rm in}$ . The variables  $\boldsymbol{W}, J_g \mathring{\boldsymbol{W}}_n, \mathring{\boldsymbol{W}}_\tau$  and the geometric quantities  $h, J_g, h, \chi$  use the initial conditions (4.3). The auxiliary quantities  $(\theta, \xi)$  are initialized as

$$\theta_j(0) = 0, \qquad \xi_j(0) = \underset{x_1 \in \mathbb{T}}{\operatorname{argmin}} \left( \frac{1+\alpha}{2} \partial_1 w_0 + \frac{1-\alpha}{2} \partial_1 z_0 + \frac{\alpha \sigma_0}{4\alpha + 2} \partial_1 s_0 \right) \Big|_{x_2 = -\pi + j\Delta x_2}, \tag{5.5}$$

where the index  $j \in \{0, 1, 2, ..., N_2 - 1\}$ . The solution to the initial value problem (5.1)–(5.5) will be referred to as the DRV-s- $N_1N_2$ , for remapped differentiated Riemann variables, or simply DRV-s- $N^2$  if  $N_1 = N_2 = N$ . Due to the smoothness of solutions to the remapped DRV system, the DRV-s- $N^2$  solutions produce 4th-order accurate approximations to the true DRV solutions.

5.1.3. The CFL condition and computational complexity. The DRV-s system has the same CFL condition for the time-step  $\Delta s$  as in (4.4); namely, we have that

$$\Delta s \left( \frac{2\alpha \|\Sigma\|_{\infty}}{J_g \Delta x_1} + \frac{\|V + 2\alpha \Sigma g^{-\frac{1}{2}} h_{,2} \|_{\infty}}{\Delta x_2} \right) \le \text{CFL},$$
(5.6)

where  $0 < \mathrm{CFL} \le 1$ . We shall again use  $\mathrm{CFL} = 1$  in our simulations. Following our definition of the numerically computed time for first singularity  $T^*_{\mathrm{num}}(N)$  in (4.6), we approximate the time of reaching the pre-shock s = 1 with the following stopping time:

$$s^*(N) = 1 - J_*,$$

where we recall that  $J_* = \Delta x_1^4$ . Following the argument which led to (4.11), the DRV-s- $N_1N_2$  algorithm has the computational complexity  $O(N_1N_2(N_1\log(N_1) + N_2))$ .

## 5.2. CSF numerical results and convergence studies.

5.2.1. Notation for DRV-s numerical solution.

**Definition 5.1** (Notation for the discretized DRV-s solution). With the nodal locations  $\mathbf{x}_{(i,j)}$  of the numerical mesh parameterized by (i,j) for i=1,...,N and j=1,...,N, we denote the DRV-s- $N^2$  solution by  $\mathbf{\Pi}_{(i,j)}^N(s)$  for  $s\in[0,s^*]$ .

**Definition 5.2** (The  $L^{\infty}$  error). For integers  $M, N \geq 4$  and  $s \in [0, s^*]$ , we set

$$\|\mathbf{\Pi}^{N}(s) - \mathbf{\Pi}^{M}(s)\|_{L^{\infty}} = \sup_{i,j} |\mathbf{\Pi}_{(i,j)}^{N}(s) - \mathbf{\Pi}_{(i,j)}^{M}(s)|.$$

Using our "flattened" spacetime coordinates (x, s), we shall again demonstrate that with  $J_*$  defined by (4.5), the DRV-s- $N^2$  solutions using the periodic initial conditions and parameters in Definition 4.4 display 4th-order accurate convergence:

$$\|\mathbf{\Pi}^N(s^*) - \mathbf{\Pi}^{512}(s^*)\|_{L^{\infty}} = O(|\mathbf{\Delta} \mathbf{x}|^4) \text{ as } |\mathbf{\Delta} \mathbf{x}| \to 0$$

5.2.2. Visualization of the uniform compression along the pre-shock set. Prior to any discussion of order of convergence, it is important to explain the fundamental effect of the spacetime transformation (3.27) which flattens the curve of pre-shocks to the single time-slice  $\{s=1\}$  (which we numerically approximate by  $\{s=s^*\}$ ). Rather than compression occurring at the spacetime location  $(y^*, T^*)$  as we displayed in the right panel of Figure 7, we instead have uniform fast characteristic impingement on the entire curve of pre-shocks as shown in Figure 13. Here, we are again using the initial conditions and parameters of Definition 4.4, we show results of our DRV-s-64 simulation for the Eulerian dominant Riemann variable  $w(y, \theta(y_2, s))$  at times s=0 (left panel),  $s=\frac{1}{2}s_*$  (middle panel), and  $s=s_*$  (right panel) for  $s^*(64)=0.99999964$ .

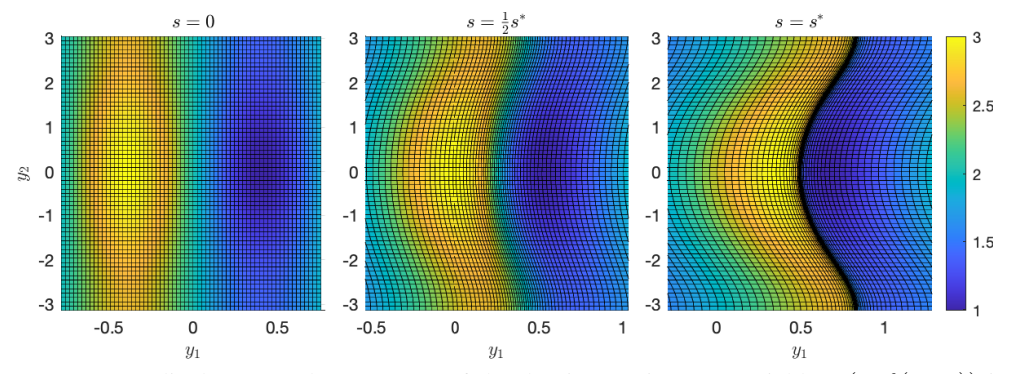


FIGURE 13. On display are color contours of the dominant Riemann variable  $w(\boldsymbol{y}, \theta(y_2, s))$  in Eulerian coordinates computed with a DRV-s- $64^2$  simulation, overlaid with rectangular mesh deformation by the ALE map  $\psi(\cdot, \theta(y_2, s))$ , shown at times s = 0,  $t = \frac{1}{2}s^*$ , and  $s = s^*$ .

5.2.3. Smoothness of the numerically computed DRV-s solution on the interval  $[0, s^*]$ . We shall next present results from a DRV-s-64 simulation using the initial conditions and parameters of Definition 4.4.

In Figure 14, which is the remapped-spacetime analogue of Figure 9, we display the ALE map  $\psi(x,s)$ , the Eulerian dominant Riemann variable w(y,s), the metric-scaled Jacobian determinant  $J_g(x,s)$ , and the ALE dominant differentiated Riemann variable  $\mathring{W}_n(x,s)$  at the approximate time of the pre-shock  $s=s^*(64)=0.99999964$ . Each panel of Figure 14 should be compared with the corresponding panel in Figure 9. In the top left panel, the image  $\psi(x,s*)$  shows the *uniform compression* of the fast acoustic wavefronts about the curve of pre-shocks. In actual time  $t\geq T^*$ , there would be a succession of gradient catastrophes, but in remapped time s, all of the first gradient blowups occur at the same time-slice, numerically approximated to be  $s=s^*$ . The top right panel shows the continuous Eulerian Riemann variable  $w(y,s^*)$ . This surface plot is smooth away from the pre-shock curve, but forms a  $C^{\frac{1}{3}}$  cusp along the Eulerian pre-shock (5.4). In the bottom left panel, we show the surface plot of  $J_g(x,s^*)$  which takes the value  $J_*$  along the entire curve  $X^*:=\{(\xi(x_2,s^*),x_2):x_2\in\mathbb{T}\}$ . Corresponding to the numerical approximation to the vanishing of  $J_g$  along the curve  $X^*$ , we display in the bottom right panel, the dominant DRV  $\mathring{W}_n(x,s^*)$  which displays approximate blowup along the entire curve  $X^*$ .

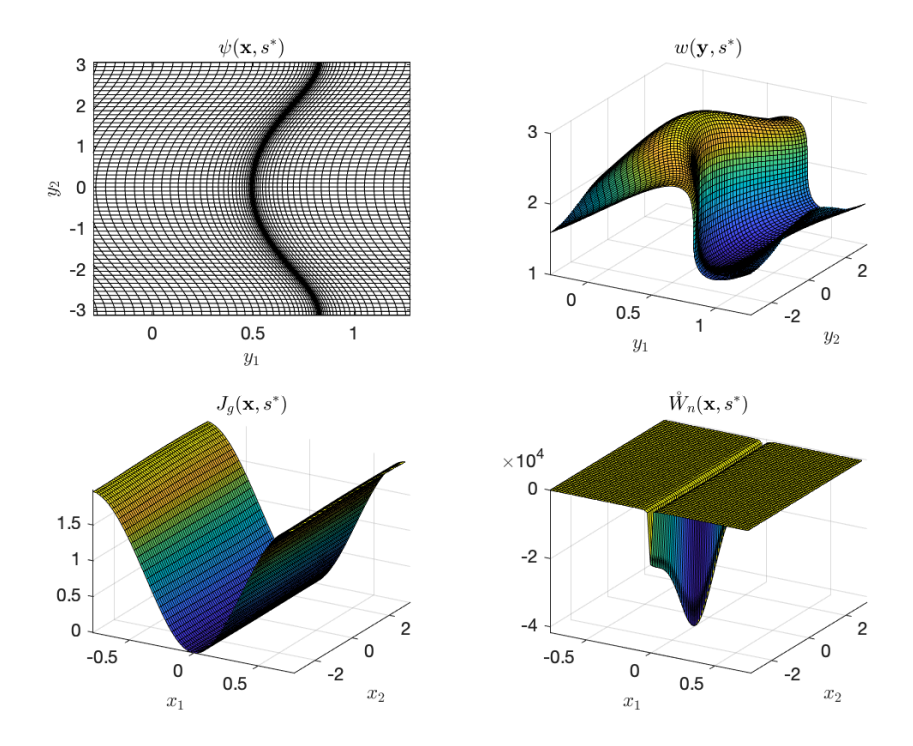


FIGURE 14. DRV-s- $64^2$  solution at the approximate time of the pre-shock  $s=s^*$ , showing the mesh deformation of the ALE map  $\psi$  (top left), the Eulerian Riemann variable w (top right), the Jacobian  $J_g$  (bottom left), and the dominant differentiated Riemann variable  $\mathring{W}_n$ . These results should be compared with the results shown in Figure 9.

5.2.4. CSF with DRV-s is 4th-order accurate. We now present a convergence study of our CSF algorithm using DRV-s- $N^2$  simulations with the initial conditions and parameters of Definition 4.4. In the left panel of Figure 15, we demonstrate the convergence  $\|\mathbf{\Pi}^N(s^*) - \mathbf{\Pi}^{512}(s^*)\|_{L^{\infty}} = O(|\Delta x|^4)$  as  $|\Delta x| \to 0$  for the specific components  $(h, W, J_g \mathring{W}_n, J_g)$  of  $\mathbf{\Pi}^N(s^*)$ .

5.2.5. Computing the fractional-order expansion at the curve of pre-shocks. The coefficients in the fractional-order expansions (3.43) and (3.44), about the pre-shock curve, are numerically computed using DRV-s- $N^2$  simulations at the time  $s = s^*(N)$  and the formulas (A.1a)–(A.2a). Derivatives are computed using the finite difference operators in Appendix A. Using these numerically computed coefficients, we define the approximate trunctated fractional-order

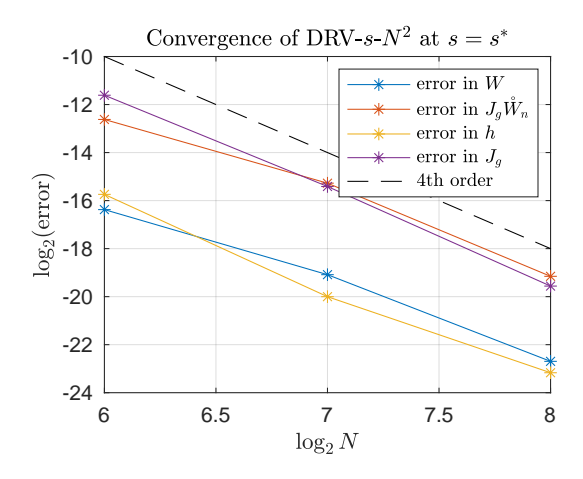


FIGURE 15. Log-log plot of  $\|\mathbf{\Pi}^{N}(s^{*}) - \mathbf{\Pi}^{512}(s^{*})\|_{L^{\infty}}$  for the components  $(h, W, J_{g}\mathring{W}_{n}, J_{g})$  of  $\mathbf{\Pi}^{N}(s^{*})$  with N = 64, 128, 256.

expansions by

$$w^*(y_1, y_2, N) = c_0^w(y_2) + c_1^w(y_2, N) (y_1 - y_1^*(y_2, N))^{\frac{1}{3}},$$
(5.7a)

$$z^*(y_1, y_2, N) = c_0^z(y_2) + c_3^z(y_2, N)(y_1 - y_1^*(y_2, N)) + c_4^z(y_2, N)(y_1 - y_1^*(y_2, N))^{\frac{4}{3}},$$
 (5.7b)

$$a^*(y_1, y_2, N) = c_0^a(y_2) + c_3^a(y_2, N)(y_1 - y_1^*(y_2, N)) + c_4^a(y_2, N)(y_1 - y_1^*(y_2, N))^{\frac{4}{3}},$$
 (5.7c)

$$s^*(y_1, y_2, N) = c_0^s(y_2) + c_3^s(y_2, N)(y_1 - y_1^*(y_2, N)) + c_4^s(y_2, N)(y_1 - y_1^*(y_2, N))^{\frac{4}{3}},$$
 (5.7d)

where

$$y_1^*(y_2,N) = h\big(\xi(y_2,s^*(N)),y_2,\theta(y_2,s^*(N))\big) \text{ and } t^*(y_2,N) = \theta(y_2,s^*(N)) \,.$$

By once again performing DRV-s- $N^2$  simulations with the initial conditions and parameters of Definition 4.4, we demonstrate in Figure 16 the 4th-order convergence of  $y_1^*(y_2, N)$ ,  $t^*(y_2, N)$ , and the coefficients in (5.7).

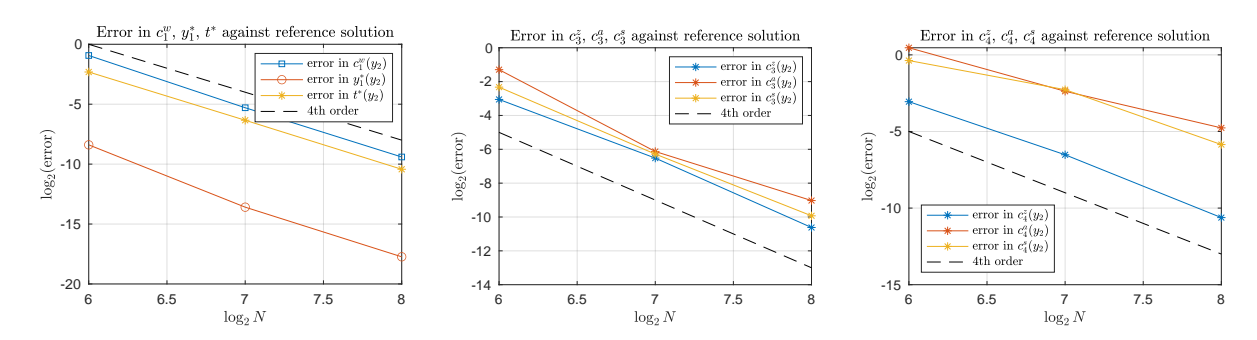


FIGURE 16. The 4th-order accurate convergence is displayed for  $y_1^*(y_2, N)$ ,  $t^*(y_2, N)$ , and the coefficients in (5.7).

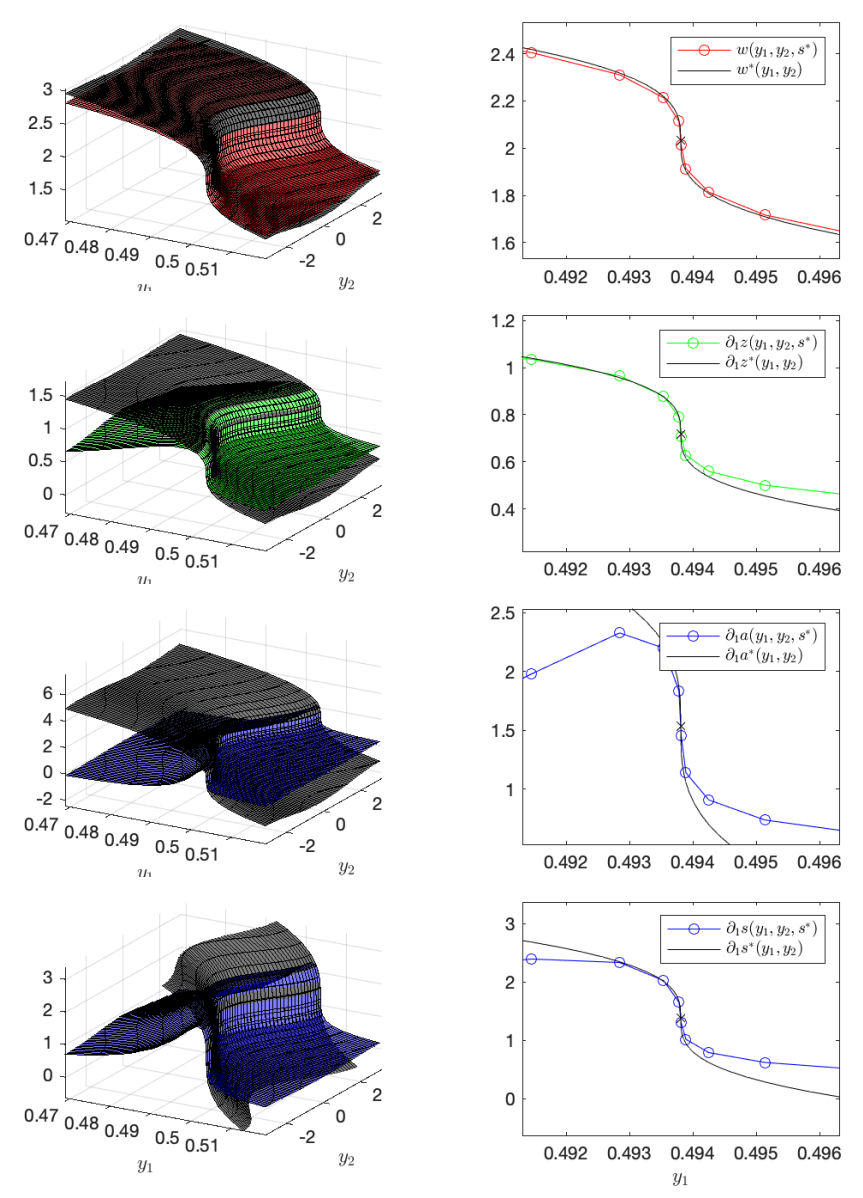


FIGURE 17. Comparison of the DRV-s-64 $^2$  solution  $w(\boldsymbol{y}, s^*)$ ,  $\partial_1 z(\boldsymbol{y}, s^*)$ ,  $\partial_1 a(\boldsymbol{y}, s^*)$ ,  $\partial_1 s(\boldsymbol{y}, s^*)$  and the functions  $w^*(\boldsymbol{y})$ ,  $\partial_1 z^*(\boldsymbol{y})$ ,  $\partial_1 a^*(\boldsymbol{y})$ ,  $\partial_1 s^*(\boldsymbol{y})$  in (5.7) computed with N=64. The panels on the right display the cross-section at  $y_2 = 0$ . The low resolution DRV-s-64 $^2$  simulation captures the  $C^{\frac{1}{3}}$  cusp structure at the pre-shock.

#### APPENDIX A. NUMERICAL COMPUTATION OF THE COEFFICIENTS OF THE PUISEUX EXPANSIONS

A.1. Numerical computation of the coefficients of the Puiseux expansions. Using DRV- $N^2$  simulations to solve (3.15)–(3.18) up to the numerically computed time of first singularity  $t = T^*_{\text{num}}(N)$  with numerically computed blowup label  $\boldsymbol{x}^*_{\text{num}}(N)$ , we define

$$\begin{split} C_0^Q &= Q(\boldsymbol{x}_{\text{num}}^*, T_{\text{num}}^*), & C_k^Q &= \frac{1}{k!} \partial_1^{k-1} (J_g \mathring{Q}_n + h,_2 J_g \mathring{Q}_\tau) (\boldsymbol{x}_{\text{num}}^*, T_{\text{num}}^*) \,, \\ C_0^h &= h(\boldsymbol{x}_{\text{num}}^*, T_{\text{num}}^*), & C_k^h &= \partial_1^{k-1} (g^{\frac{1}{2}} J_g) (\boldsymbol{x}_{\text{num}}^*, T_{\text{num}}^*) \,, \end{split}$$

for  $k=1,\ldots,4$  and where the variable Q is either W,Z,A or S and the variable  $\mathring{Q}$  is either  $\mathring{\boldsymbol{W}},\mathring{\boldsymbol{Z}},\mathring{\boldsymbol{A}}$ , or  $\mathring{\boldsymbol{S}}$ . The coefficients in (3.22) are then computed as follows:

$$c_0^w = C_0^W,$$
  $c_1^w = (C_3^h)^{-\frac{1}{3}} C_1^W,$  (A.1a)

and

$$c_0^q = C_0^Q,$$
  $c_3^q = (C_3^h)^{-1}C_3^Q,$   $c_4^q = (C_3^h)^{-\frac{4}{3}}(C_4^Q - C_3^Q C_4^h/C_3^h),$  (A.1b)

for  $q \in \{z, a, s\}$ . The coefficients in (3.23) are given by

$$c_0^{u_1} = U^1(\boldsymbol{x}_{\text{num}}^*, T_{\text{num}}^*), \qquad c_0^{u_2} = U^2(\boldsymbol{x}_{\text{num}}^*, T_{\text{num}}^*), \quad c_0^{\sigma} = \Sigma(\boldsymbol{x}_{\text{num}}^*, T_{\text{num}}^*), \quad (A.2a)$$

$$c_{1}^{u_{1}} = \frac{1}{2}g(\boldsymbol{x}_{\text{num}}^{*}, T_{\text{num}}^{*})^{-\frac{1}{2}}c_{0}^{w}, \quad c_{1}^{u_{2}} = \frac{1}{2}g(\boldsymbol{x}_{\text{num}}^{*}, T_{\text{num}}^{*})^{-\frac{1}{2}}h_{,2}(\boldsymbol{x}_{\text{num}}^{*}, T_{\text{num}}^{*})c_{0}^{w}, \qquad c_{1}^{\sigma} = \frac{1}{2}c_{0}^{w}. \quad (A.2b)$$

The 4th-order finite difference stencils needed to compute the second and third derivatives are given by

$$\begin{split} D_1^{(2)}F(i,j) &= \frac{-F(i-2,j) + 16F(i-1,j) - 30F(i,j) + 16F(i+1,j) - F(i+2,j)}{12\Delta x_1^2}, \\ D_1^{(3)}F(i,j) &= \frac{F(i-3,j) - 8F(i-2,j) + 13F(i-1,j) - 13F(i+1,j) + 8F(i+2,j) - F(i+3,j)}{2\Delta x_1^3}, \end{split}$$

A.2. Coefficients of the fractional-order expansions at the pre-shock. Using DRV-s- $N^2$  simulations, to solve (3.37)–(3.39) up to  $s = s^*(N)$ , we define

$$C_0^Q(y_2) = Q(\xi(y_2, s^*), y_2, s^*), \qquad C_k^Q = \frac{1}{k!} \partial_1^{k-1} (J_g \mathring{Q}_n + h,_2 J_g \mathring{Q}_\tau) (\xi(y_2, s^*), y_2, s^*),$$

$$C_0^h(y_2) = h(\xi(y_2, s^*), y_2, s^*), \qquad C_k^h = \partial_1^{k-1} (g^{\frac{1}{2}} J_g) (\xi(y_2, s^*), y_2, s^*),$$

for k = 1, ..., 4. The coefficients in (3.43)–(3.45) are once again defined by (A.1a)–(A.2a), now regarded as functions of  $y_2$ . Again, for DRV-s- $N^2$  simulations, the numerically computed temporal coordinate along the pre-shock  $t^*(y_2, N)$  and the numerically computed spatial coordinate along the pre-shock  $y_1^*(y_2, N)$  are given by

$$t^*(y_2, N) = \theta(y_2, s^*(N))$$
 and  $y_1^*(y_2, N) = h(\xi(y_2, s^*(N)), y_2, \theta(y_2, s^*(N)))$ .

### ACKNOWLEDGEMENTS

The work of S.S. and V.V. was supported in part by the Collaborative NSF grant DMS-2307680. This work is supported by the Laboratory Directed Research and Development Program (20230120DR) of the Los Alamos National Laboratory, which is under the auspices of the National Nuclear Security Administration of the U.S. Department of Energy under DOE Contracts W-7405-ENG-36 and LA-UR-10-04291. This research was also supported by Office of Defense Nuclear Nonproliferation Research and Development NA-22.

### REFERENCES

- [1] Tristan Buckmaster, Theodore D. Drivas, Steve Shkoller, and Vlad Vicol. Simultaneous development of shocks and cusps for 2D Euler with azimuthal symmetry from smooth data. *Annals of PDE*, 8(2):1–199, 2022.
- [2] Tristan Buckmaster, Steve Shkoller, and Vlad Vicol. Formation of shocks for 2D isentropic compressible Euler. Comm. Pure Appl. Math., 75(9):2069–2120, 2022.
- [3] Tristan Buckmaster, Steve Shkoller, and Vlad Vicol. Formation of point shocks for 3D compressible Euler. Comm. Pure Appl. Math., 76(9):2073–2191, 2023.
- [4] Tristan Buckmaster, Steve Shkoller, and Vlad Vicol. Shock formation and vorticity creation for 3D Euler. Comm. Pure Appl. Math., 76(9):1965–2072, 2023.
- [5] L. D. Landau and E. M. Lifshitz. Course of theoretical physics. Vol. 6. Pergamon Press, Oxford, second edition, 1987. Fluid mechanics, Translated from the third Russian edition by J. B, Sykes and W. H. Reid.
- [6] Isaac Neal, Steve Shkoller, and Vlad Vicol. A characteristics approach to shock formation in 2d euler with azimuthal symmetry and entropy, 2023.
- [7] Raag Ramani and Steve Shkoller. Computational shock development: accurately resolving cusps and discontinuities in the 1D Euler equations. arXiv preprint, 2024.
- [8] Steve Shkoller and Vlad Vicol. The geometry of maximal development and shock formation for the Euler equations in multiple space dimensions. *Inventiones mathematicae*, 237(3):871–1252, 2024.

DEPARTMENT OF MATHEMATICS, UNIVERSITY OF CALIFORNIA DAVIS, DAVIS, CA 95616.

Email address: gpandya@math.ucdavis.edu

DEPARTMENT OF MATHEMATICS, UNIVERSITY OF CALIFORNIA DAVIS, DAVIS, CA 95616.

Email address: shkoller@math.ucdavis.edu

COURANT INSTITUTE OF MATHEMATICAL SCIENCES, NEW YORK UNIVERSITY, NEW YORK, NY 10012.

Email address: vicol@cims.nyu.edu